Pneumatic conveying of cohesive dairy powder
Experiments and CFD-DEM simulations

Olaleye, Akeem K.; Shardt, Orest; Walker, Gavin M.; Van den Akker, Harry E.A.

DOI
10.1016/j.powtec.2019.09.046

Publication date
2019

Document Version
Final published version

Published in
Powder Technology

Citation (APA)
Olaleye, A. K., Shardt, O., Walker, G. M., & Van den Akker, H. E. A. (2019). Pneumatic conveying of cohesive dairy powder: Experiments and CFD-DEM simulations. *Powder Technology*, *357*, 193-213. https://doi.org/10.1016/j.powtec.2019.09.046

Powder Technology 357 (2019) 193–213

Contents lists available at ScienceDirect

Powder Technology

journal homepage: www.elsevier.com/locate/powtec

Pneumatic conveying of cohesive dairy powder: Experiments and CFD-DEM simulations

Akeem K. Olaleye [a,b,*], Orest Shardt [a], Gavin M. Walker [a,b], Harry E.A. Van den Akker [a,b,c]

[a] The Bernal Institute, University of Limerick, Limerick, Ireland
[b] Dairy Processing Technology Centre (DPTC), The Bernal Institute, University of Limerick, Limerick, Ireland
[c] Department of Chemical Engineering, Delft University of Technology, Delft, the Netherlands

ARTICLE INFO

Available online 3 October 2019

Keywords:
Pneumatic conveying
Cohesive dairy powder
Computational fluid dynamics
Discrete element
Method

ABSTRACT

We performed an experimental and numerical investigation of pneumatic conveying of cohesive dairy powder. The experiments with fat-filled milk powder (FFMP) fines with an average particle size of 94 μm were carried out in a 2-inch diameter stainless steel pipe consisting of two 2.5 m horizontal sections connected to a 0.65 m vertical section by two bends of 0.4 m radius each. In addition to measurements of pressure drop and powder deposition, an optical technique was used to measure the dynamics (probability densities) of local particle volume fractions as a function of operating conditions. Numerical simulations were performed with a commercial discrete element modelling (DEM) software, EDEM®, coupled with the computational fluid dynamics (CFD) software, FLUENT®. The simulation results in terms of pressure drops and particle volume fractions were compared with the experimental data. A very satisfactory agreement was found. At low gas velocities, cohesive dairy powders easily re-agglomerate after the second 90° bend and then deposit at the bottom of the horizontal pipe. At higher gas velocities, results show intermittent dispersion of particles and less particle deposition is observed even at higher loading ratio.

1. Introduction

1.1. Pneumatic conveying of cohesive milk powder

Dairy powders are generally soft and sticky. They are produced from a series of processing steps from milk intake to the final product packaging. Powder transport plays an important role in dairy processing, particularly in post-drying stages, during silo filling or emptying, and in packaging operations [1]. Mechanical and pneumatic transport systems are the most common means of conveying dairy powders depending on factors such as location, sources, and destination of the powders. Pneumatic conveying has many advantages over mechanical conveying such as reduced spillage and powder loss, low product contamination, and low cost of maintenance [1].

One critical area of application for pneumatic conveying in the dairy industry is in fines return systems. Fines return systems are used to achieve good agglomeration and reduce energy consumption during spray drying of cohesive dairy powders [1] such as fat-filled milk powder (FFMP) fines. Dilute phase pneumatic conveying is usually preferred for transporting fines into the atomizing zone of the spray dryer to achieve intimate contact with the sprayed droplets [1]. FFMP fines are one of the most problematic powders to convey even in dilute phase systems due to the presence of fat, its cohesiveness, and particle size smaller than 100 μm.

Previous studies on the pneumatic conveying of dairy powders have focused on the measurement of macro-scale system variables, such as the effects of conveying parameters on milk powder breakage [2,3], of milk powder properties on breakage [4], and of conveying system characteristics on gas velocity [5]. These effects may be the result of a combination of fluid-particle (F–P), particle-particle (P–P) and particle-wall (P–W) interactions, such as formation of particle clusters, powder deposition, powder re-entrainment and powder breakage, often leading to particle clogging and even pipeline blockages. It is difficult to disentangle the combined effects by means of macro-scale experimental studies. More reliable and accurate techniques are needed to analyse, understand and unravel all these interactions. Various non-intrusive techniques such as electrical capacitance tomography (ECT) [6,7] and optical measurements [8–13] have been applied to the pneumatic conveying of bulk solids.

---

[*] Corresponding author. The Bernal Institute, University of Limerick, Limerick, Ireland.
E-mail address: Akeem.Olaleye@ul.ie (A.K. Olaleye).

https://doi.org/10.1016/j.powtec.2019.09.046
0032-5910/

Optical measurement techniques are based on resolved imaging of particles, attenuation of transmitted light or a Doppler shift. An example of the resolved imaging is particle image velocimetry (PIV) [8], while techniques exploiting a Doppler shift include Doppler anemometry (LDA) [9] and phase Doppler anemometry (PDA) [10]. Most Doppler-based optical techniques are expensive. In contrast, the light attenuation principle can be applied at a lower cost than laser Doppler velocimeters. Several studies have been conducted with an attenuation-based optical technique using a halogen lamp or an LED light source coupled with a photodiode sensor to measure loading and flow fluctuations in transport of fine and coarse particles [11–13]. The current study uses an LED light source fitted with a fibre-optic light guide, coupled with a photodiode sensor to measure the pneumatic conveying characteristics of a cohesive milk powder. In contrast to previous studies on fluctuations in coal conveying [11,12], optical measurements of the pneumatic conveying of cohesive dairy powders have not been reported in the open literature.

Bends are very common in pipe networks for pneumatic transport, especially due to space limitation and re-routing of pipe networks. They are known to be responsible for gas-solid flow structures common in cohesive powder transport such as particle roping, deposition, dispersion and clogging. Most of the optical measurement techniques have focused on horizontal pneumatic conveying lines [6,8–10], while others included a single 90° bend [12], double 90° bends [13], and multiple 90° bends [7] in horizontal-to-vertical (H–V) and vertical-to-horizontal (V–H) pipe arrangements. The current study focuses on the three most common bend orientations were studied i.e. H–V, V–H and the horizontal-to-horizontal (H–H). The effects of these bends on cohesive powder transport were investigated.

Experiments, however, are generally difficult to upscale, and too expensive for optimization and/or design studies. An effective research approach is to exploit a numerical tool, to validate it with a limited number of experiments, and then to numerically analyse the influence of cohesive powder properties on the performance of a pneumatic conveying system. By doing this, answers may be found to various important fundamental questions — for example, to what degree are inter-particle cohesive forces affecting the conveying characteristics of dairy powders? What effect does the presence of a cohesive dairy powder have on the hydrodynamic characteristics of a pneumatic conveying system? It is hard to obtain answers to these questions from experimental studies due to the difficulty in measuring and controlling the cohesive powder's P–P and P–W interaction forces quantitatively in experiments.

A coupled CFD-DEM numerical approach can overcome this issue. DEM has been effective in describing dynamics of particulates in bulk solids handling devices such as in pneumatic transport lines [9,14], cyclone separators [15] and fluidized beds [16–19]. This approach has recently been advanced from non-cohesive to cohesive particle dynamics, mostly for fluidized beds however [20,21]. Just a few studies on turbulent flow laden with very fine cohesive particles (as in aerosols) exploited DEM, either coupled to Large Eddy Simulations (LES) [22,23] or to Reynolds Averaged Navier-Stokes (RANS) based flow simulations [24].

The objective of this study was to analyse the influence of conveying parameters on cohesive dairy powder deposition during pneumatic conveying. To this end, a pneumatic conveying test rig was constructed to measure local volume fraction using a fibre-optical measurement technique, while also differential pressure and powder deposition were measured. A CFD-DEM simulation approach was developed and validated with experimental results.

1.2. Forces in pneumatic conveying of cohesive powders

Three distinctive relationships affect the flow characteristics of cohesive powders in pneumatic conveying systems: fluid-particle (F–P), particle-particle (P–P), and particle-wall (P–W) interactions. Fluid-particle interaction forces [25,26] include particle-fluid drag force, lift force, and other un-steady forces (i.e. virtual mass force, Basset force). We considered only drag and lift forces.

During pneumatic conveying, P–P and P–W interactions are due to mutual collisions between particles and due to particles impinging onto and sticking to the enclosing pipe, respectively. In dilute phase conveying of non-cohesive particles, the effect of P–P interactions is negligibly small compared to that of F–P interactions, while cohesive particles often result in significant P–P interactions (agglomeration) as well as P–W adhesion (deposition). Cohesive interactions are attributed mainly to London-Van der Waals forces the origin of which is in momentary electric and magnetic fields occurring spontaneously on and between particles and the wall surface [27]. The effect of P–W and P–P interactions is very important in predicting cohesive particle flow even in dilute phase systems and is the main topic of this paper.

2. Experimental method

2.1. Test rig

The pneumatic conveying test rig (see Fig. 1) consisted of several 2-inch diameter 316L stainless steel pipes of varying length (650 and 960 mm), with horizontal and vertical sections connected by two 90° bends with a 400 mm radius. This scale was selected to provide a close analogue of a dairy industry conveying system, where 2–3.5-inch diameter pipes are used to transport cohesive fines from the fluidized bed back to the top of the spray dryer. The powder was supplied to the loop, at the upstream horizontal end, via an open funnel by using a vibrating gutter, while at the downstream end of the line the powder was collected in a plastic bucket fitted with air filters. The rig was provided with four in-line sight-glasses to allow visual observation of the powder transport operation, viz. at the feed point, after the two 90° bends, and upstream of the powder receiving hopper. Air pressure was regulated to provide different velocities. A differential pressure sensor is installed at two positions on the rig, viz. at the powder feeder and upstream of the powder receiving bucket. Superficial gas velocities were calculated from pressure drop measurements when operated with air only.

The fraction of the pipe cross-section occupied by the passing powder, denoted as the *volume fraction,* is measured with the aid of a fibre optics probe. The probe was positioned horizontally at three different sections on the rig: on the vertical pipe, on the horizontal pipe, and at the upstream of the powder receiving hopper (7). Fig. 2 shows the schematics of the fibre-optic probes and the photodiode receiver used in this study.

The light transmitted from the fibre optics is detected and converted to voltage by using a photo-diode receiver (6). A data acquisition (DAQ) unit and a pc, (9) and (10) in Fig. 1, were installed to record and process the optical-electrical signals from the photo-diode receiver. The DAQ system records the changes in voltage based on the concentration of particles passing through the sensors. The data recorded was processed using MATLAB®. The voltage measurement was converted to a chord length averaged volume fraction (based on the light intensity detected, particle density, and path length of the light) using the Lambert-Beer correlation thus:

To model the dependence of the light intensity on the solids volume fraction, we follow the Lambert-Beer law and write as in eq. (1) thus:

$$-\ln\frac{I}{I_o} = A_s\phi \tag{1}$$

where I is the measured intensity, I_o is the intensity in the absence of any solids ($\phi = 0$), and A_s is the model constant. All the measured intensities

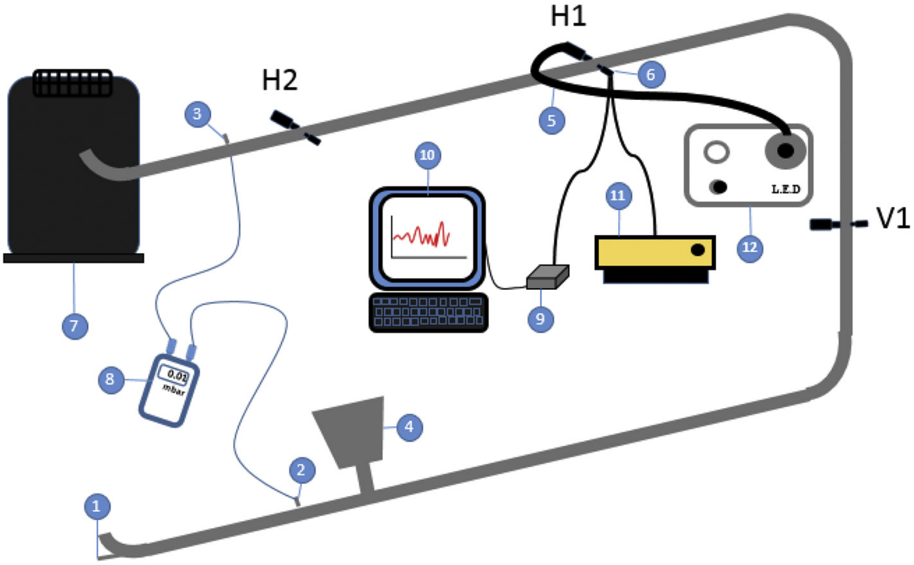

Fig. 1. Pneumatic Conveying Rig Setup: (1) compressed air, (2) pressure tapping 1, (3) pressure tapping 2, (4) powder feeder, (5) fibre optics light guide, (6) photo-diode receiver, (7) Receiving hopper with air filter, (8) differential pressure meter, (9) data acquisition unit, (10) computer, (11) photo-diode power supply, and (12) fibre optic light source.

are averaged over the chord length and converted to voltage readings by the photodiode module.

The I_o is measured in an empty pipe ($\phi = 0$). Using the transmitted light intensity, I_{min}, when the pipe is filled with FFMP ($\phi = \phi_{max} \cong 0.58$), we find the value of A_s thus in eq. (2):

$$A_s = \frac{-1}{\phi_{max}} \ln \frac{I_{\min}}{I_o} \tag{2}$$

Powder deposition on the pipe wall was measured in the rig by analysing the weight of the powder deposited on the walls of the pipe (i.e. at bends) after each run of the experiment and was expressed as a fraction of the amount of powder fed.

2.2. Test materials

Fat-filled milk powder (FFMP) fines was used for this study with compositions of 24% fat, 26% protein, 39% lactose, 6% minerals and 3–4% moisture. The fines have an average particle size of 93 μm. Table 1 shows a summary of the physical properties of the FFMP fine powder used in this study.

2.3. Test conditions

Design of experiments (DOE) offers a practical approach for exploring multi-factor operating scenarios (i.e. varying air and/or powder conveying conditions) in a fines transport line, and the response of the system and/or powder (i.e. pressure drop, powder deposition, volume fraction) to these factors. The DOE method used in this study is a factorial design based on the Taguchi method of analysis [28]. It is used to consider the responses (e.g. pressure drop, volume fraction, bulk density, particle size distribution etc.) of a system to changes in several input parameters such as air velocity, solid loading, powder feed rate (G_{solid}), length of horizontal pipes (L_H), length of vertical pipes (L_V), radius of bends (R_B) at different factor levels. In this study, only two factors, viz. G_{solid}, V_{air} were considered. Both factors were controlled at two levels (high - *level 1*, and low – *level 2*). Table 2 shows the sequence of experimental runs.

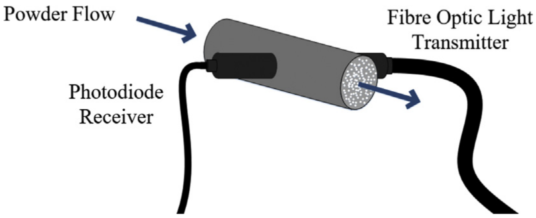

Fig. 2. Optical fibre light source and photodiode receiver.

Table 3 shows the actual experimental runs with the associated values of the input variables. Three responses (i.e. pressure drop, volume fraction at three locations, and powder deposition) were evaluated for all runs as detailed in the results sections.

The solid feed rates and air velocities have been selected by translating industrial operation conditions into a solid loading ratio of 0.0272, where the loading ratio is defined as the ratio of the mass flow rate of powder to the mass flow rate of air. The variations in air velocity and powder feed rate correspond to within ±60% of the solid loading ratio of a typical industrial scale dairy fines return systems (i.e. *0.018 to 0.045*).

The measurement of local particle volume fraction was obtained at three different locations (Fig. 3) on the rig by using a single fibre-optic probe. The locations were V1, on the vertical section after the first 400 mm radius (H–V) bend, H1 at the horizontal section immediately after the second 400 mm radius bend (V–H), and H2

Table 1
FFMP fines physical properties.

Parameter	Value	Units	Measuring instrument
Particle size Distribution (PSD) $[d_{10}]$	37.7	μm	Microtrac® particle size analyser
$[d_{50}]$	93.5	μm	
$[d_{90}]$	183.7	μm	
Span $[(d_{90} - d_{10})/d_{50}]$	1.56	[−]	
Particle shape	–	–	Scanning electron microscopy (SEM)
Particle Density	1187	kg/m^3	Gas pycnometer
Bulk Density	510	kg/m^3	FT4 powder rheometer
Angle of Internal friction	18.3	degree	FT4 powder rheometer
Wall friction angle	23.2	degree	FT4 powder rheometer
Surface Energy	160	mJ/m^2	Attension® Theta Optical tensiometer

Table 2
Sequence of experimental runs.

RUNS	V_{air}	G_{solid}
R1	2	2
R2	2	1
R3	2	2
R4	1	2
R5	1	2
R6	2	1
R7	1	1

Table 3
Final DOE for the conveying experiments.

Factors		
RUNS	V_{air} (m/s)	G_{solid} (g/s)
R1(R3)	11.5	0.5
R2(R6)	11.5	1.1
R5(R4)	16.5	0.5
R7(R8)	16.5	1.1

just upstream of the H–H bend, at axial distances of 7D, 11D, and 14.2D (*where D is pipe diameter*) from the feeder, respectively.

3. Numerical simulation

3.1. Introduction

Describing the translational and rotational motions of discrete particles immersed in a fluid phase requires knowledge of all particle-particle, particle-wall and particle-fluid interaction forces (i.e. contact/non-contact). Generally, the discrete element method (DEM) first proposed by Cundall and Strack [29] is used to describe such motions, based on laws of motion applied to individual particles. On the other hand, computational fluid dynamics (CFD) is used to describe the flow of the carrier fluid based on the local averaged Navier-Stokes equations. Coupling the fluid modelling strengths of CFD with the prowess of DEM results in the combined CFD-DEM modelling approach capable of dealing with all relevant interactions. It was first proposed by Tsuji et al. [30,31]. Zhu et al. [32] emphasized the attractiveness of CFD-DEM over two-fluid modelling for describing the detailed dynamics of the particle behaviour.

In this study on pneumatic conveying of cohesive particles, simulations were carried out by means of the commercial CFD solver, Ansys FLUENT® and the commercial DEM solver, EDEM®, coupled in a Eulerian-Langrangian framework (Fig. 4). The Reynolds Averaged Navier-Stokes (RANS) equations are solved in FLUENT® for the gas phase, supplemented with the standard k-ε turbulence model with enhanced wall treatment, by using a finite volume discretisation scheme and by applying an iterative solution procedure based on the Coupled SIMPLE algorithm [26].

The RANS approach is preferred over large eddy simulation (LES), since LES computation would be prohibitive when coupled with DEM for the scale considered. A k-ε turbulence model is commonly used for internal flows as it provides a good approximation of the flow turbulence. It may also be sufficiently accurate because the flow is dominated by the P–P and P–W interaction forces due to the size of the particles (~90 μm) and their mechanical properties (i.e. surface energy, non-spherical shapes). This is particularly the case at even low loadings of cohesive solids due to the effects of increased number and intensity of particle-wall and inter-particle collisions on particle deposition and clustering. A quantitative comparison of the magnitudes of these interaction forces for typical cases are presented in Appendix A. For the same reason, the effect of turbulence modulation as described in Ebrahimi and Crapper [33], was not considered in this study.

The motion of the particle phase is described by solving Newton's and Euler's laws of motion for individual particles. The two solvers are coupled with full momentum exchange between the particle and gas phases. EDEM® integrates fluid drag forces and torques into the particle simulation on an individual particle level. When EDEM® performs a step of the simulation, the external forces act upon the particles in addition to any gravitational or collision forces. Fig. 4 depicts the stages of the EDEM simulation loop including the point at which it interacts with the CFD solver [22].

3.2. Governing equations

3.2.1. Fluid phase (CFD)

The flow of a gas phase is governed by volume-averaged mass and momentum conservation equations in each fluid cell, as derived by Anderson and Jackson [34]. The time dependent 3D mass and momentum

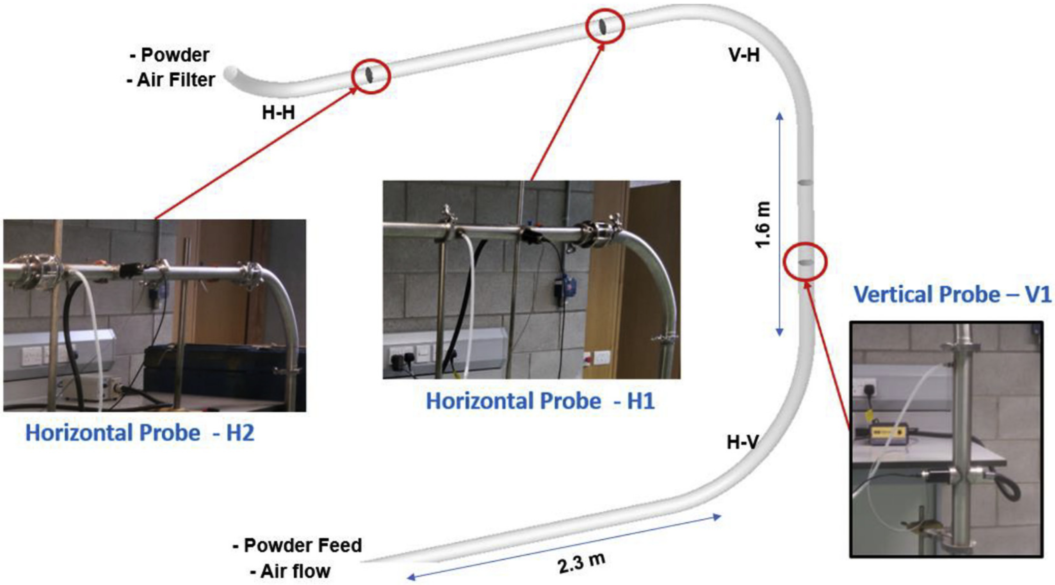

Fig. 3. Locations of the fibre-optics probes on the Conveying rig.

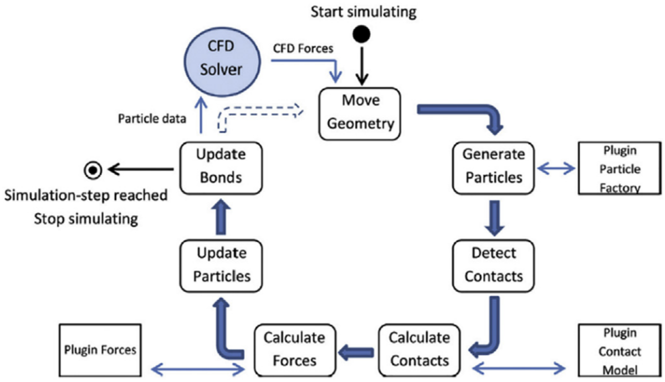

Fig. 4. Coupling scheme of the CFD-DEM Model in EDEM-FLUENT [22].

conservation equations can be expressed as shown in eq. (3) and eq. (4), respectively [9, 35]:

$$\frac{\partial(1-\phi)\rho}{\partial t}+\nabla\cdot(1-\phi)\rho\mathbf{u}=0 \tag{3}$$

$$\frac{\partial(1-\phi)\rho\mathbf{u}}{\partial t}+\nabla\cdot(1-\phi)\rho\mathbf{u}\mathbf{u}=-(1-\phi)\nabla p+\nabla\cdot((1-\phi)\tau)$$
$$+(1-\phi)\rho g-S$$

$$S=\frac{\sum_i^{n_m}F_{F-P,i}}{\Delta V_{mesh}} \tag{5}$$

where $\boldsymbol{\tau}, n_m, \Delta V_{mesh}$ represent the fluid viscous stress tensor, the number of particles in the mesh cell, and the computational cell volume respectively. For turbulent flow, a so-called Reynolds stress term must be added to eq. (4). The term S in eq. (5) is the volumetric force in each mesh cell, where the drag and lift forces are comprised in $F_{F-P,i}$.

The dominant F–P forces are the drag and the lift forces [36], while all other forces such as the added mass and the Basset force are negligible for the density ratio considered. Due to the non-spherical shape of the dairy powder particles, the Haider and Levenspiel [37] drag model is used in this study to describe the F–P drag force:

$$C_D=\frac{24}{\mathrm{Re}_{sph}}\left(1+b_1\mathrm{Re}_{sph}^{b_2}\right)+\frac{b_3\mathrm{Re}_{sph}}{b_4+\mathrm{Re}_{sph}} \tag{6}$$

where,

$$Re_{sph}=\frac{\rho_f|\mathbf{u}-\mathbf{v}|d_p}{\mu} \tag{7}$$

$$b_1=\exp\left(2.3288-6.4581\varnothing^2\right) \tag{8}$$

$$b_2=0.0964+0.5565\varnothing \tag{9}$$

$$b_3=\exp(4.905-13.8944\varnothing+18.4222\varnothing^2-10.2599\varnothing^3 \tag{10}$$

$$b_4=\exp\left(1.4681-12.2584\varnothing+20.7322\varnothing^2-15.8855\varnothing^3\right) \tag{11}$$

in which C_D eq. (6), Re_{sph} eq. (7), $\varnothing$ in eq. (8, 9, 10 and 11) represent the drag coefficient, the Reynolds number based on the diameter of a particle having the same volume, and Corey's shape factor, respectively. Corey's shape factor [38] is defined as the *ratio of the length of the shortest particle axis to the square root of the product of those of the other two axes*. This factor expresses that all three axes affect the settling velocity of a particle, with the short axis affecting it more than the others because it presents the highest deviation from a spherical particle.

Corey's shape factor is expressed in eq. (12) thus:

$$\varnothing=\frac{c}{\sqrt{(ab)}},a>b>c \tag{12}$$

in which $a, b,\ c$ represent the lengths of the three principal axes of the particle. Fig. 5(a) shows the shape of a typical (agglomerated) FFMP particle and the three principal axes. Based on the Corey shape factor calculation, a value of 0.565 was estimated for the FFMP fines.

We took two types of lift forces into account. First, we considered the shear induced lift force due to its significance in the viscous sub-layer at the pipe wall with high velocity gradients acting on the surface of the particle, thereby causing lift [39]. The lift force has been proven to be of great importance in the investigation of particle deposition over the wall [40]. It was estimated using the Saffman lift correlation which can be expressed as [41]:

$$F_{Saff}=1.61d_p^2\left(\mu_f\rho_f\right)^{1/2}|\omega_c|^{-1/2}[(\mathbf{u}-v)]\times\boldsymbol{\omega}_c \tag{13}$$

where $\boldsymbol{F}_{Saff},\ d_p, \mu_f, \rho_f, \boldsymbol{\omega}_c, \boldsymbol{u}$, and $\boldsymbol{v}$ in eq. (13) are the lift force, particle diameter, fluid viscosity, fluid density, vorticity of the flow, gas velocity and particle velocity respectively. The second lift force is the Magnus or rotational lift force which arises when a particle is rotating in a fluid. It is caused by a pressure differential along the

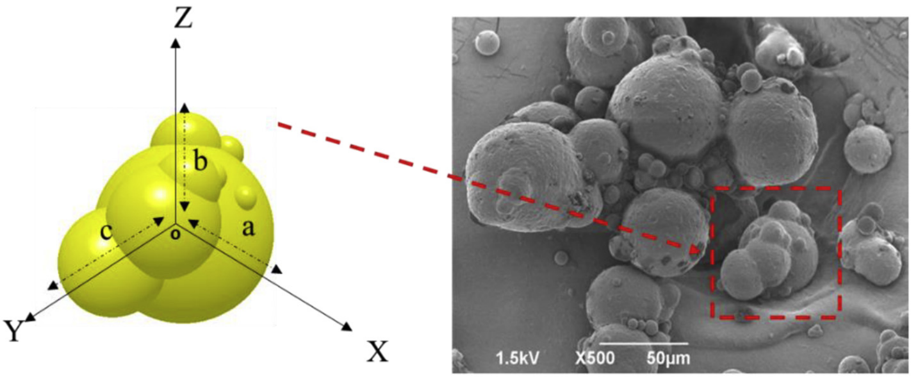

Fig. 5. (a) modelled FFMP particle (b) SEM image of the particle.

particle's surface [26]. The Magnus lift force can be expressed as in eq. (14):

$$\boldsymbol{F}_{Mag} = 0.125\pi d_p^3\,\rho_f \frac{Re_{sph}}{Re_\Omega} C_L[(0.5\boldsymbol{\omega}_c - \boldsymbol{\omega}_p) \times (\boldsymbol{u} - \boldsymbol{v})] \tag{14}$$

where $\boldsymbol{F}_{Mag}$, $d_p, \rho_f, Re_\Omega, \boldsymbol{\omega}_p, \boldsymbol{u}$, and $\boldsymbol{v}$ are the rotational lift force, particle diameter, fluid density, rotational particle Reynolds number, particle angular velocity, gas velocity and particle velocity respectively. The rotational lift coefficient, C_L, in eq. (15) is estimated from:

$$C_L = 0.45 + \left(\frac{\mathrm{Re}_{sph}}{\mathrm{Re}_\Omega} - 0.45\right)\exp\left(-0.05684\mathrm{Re}_\Omega^{0.4}\mathrm{Re}_{sph}^{0.3}\right) \tag{15}$$

This model is valid for Re_{sph} up to 2000 [39].

3.2.2. Particle phase (DEM)

Given a particle, i with mass m_i and moment of inertia I_i, its motion (i.e. translational and rotational) can be expressed as follows [32]:

$$m_i \frac{dv_i}{dt} = \sum_j F_{ij}^c + \sum_k F_{ik}^{nc} + F_i^f + F_i^g \tag{16}$$

$$I_i \frac{d\boldsymbol{\omega}_i}{dt} = \sum_j \boldsymbol{M}_{ij} \tag{17}$$

where $m_i, I_i, v_i, \boldsymbol{\omega}_i$, are the mass, moment of inertia, translational velocity, and the rotational velocity. The interacting forces are: the gravitational force F^g, the contact force $\boldsymbol{F}_{ij}^{\boldsymbol{c}}$, non-contact force F_{ik}^{nc}, acting on particle i by particle k or walls, and the fluid-particle forces, $\boldsymbol{F}^f$. Solving eq. (16) and eq. (17) is key in describing the dynamics of particles in motion.

The total P–P and P–W forces between cohesive particles can be attributed to both contact forces and non-contact forces. The non-contact forces may originate from sources such as the liquid bridge force, van der Waals force, electrostatic force, or magnetic force. In this study, the focus is on the van der Waals interactions between cohesive particles and between a particle and a wall. The issue with soft (fatty) and cohesive particles is that on contacting or colliding, the area around the contact 'point' becomes flattened, as a result of which the van der Waals forces become relevant. The theory assumes that two particles in contact only feel an attractive force across the flattened contact area with radius a, while the particle surfaces outside this flattened contact area are force free [42].

Johnson et al. [43] modified the Hertzian contact model to include the effect of attractive forces (adhesion) between two attractive bodies (see Table 4). The theory calculates the increase in contact area due to attraction between the attracting bodies. According to the JKR theory, the adhesive force is related to the surface-energy interactions (van der Waals interactions) between two spheres in contact. It is proportional to surface energy and the radius of curvature at the contact (Table 4).

Table 4 summarises the basic equations of the HM-JKR contact force models. The HM-JKR (an *elastic-adhesive contact*) model calculates the normal cohesive contact force between particles based on the Van der waals forces. It also calculates particle-wall adhesion between fine dry powders and the geometry of interest. Previous work on CFD-DEM of dilute phase pneumatic conveying like [9,33] used the HM contact model only. In this study, the HM-JKR contact model is implemented for P–P cohesion of the FFMP fines and the P–W adhesion to the stainless-steel pipe of the conveying system.

Table 4
Contact Model used in DEM for the cohesive powder.

Force Models			
Contact ($\boldsymbol{F}^c$)	Normal Force (F_n)	Tangential Force (F_t)	Reference
Hertz-Mindlin (HM) with JKR Cohesion (HM-JKR)	JKR normal force depends on surface energy (γ), the overlap (δ), and interaction parameter thus: $F_{JKR} = -4\sqrt{\pi\gamma E^*}\,a\frac{3}{2} + \frac{4E^*}{3R^*}a^3$ $\delta = \frac{a^2}{R^*} - \sqrt{4\pi\gamma/E^*}$	$F_t = -S_t\delta_t$ where, $S_t = 8G^*\beta\sqrt{R^*\delta_n}$	[42]

3.3. Simulation conditions

3.3.1. CFD-DEM parameters configuration

The computational domain simulated in this study is the piping section of the test rig (shown in Fig. 3), leaving out the powder feeder, the receiving hopper, and the air filter. The three H–V, V–H and H–H bends were included in the simulated cases. Table 5 gives the simulation parameters for the four experimental conditions simulated. In the simulations, the FFMP particles were released in the horizontal pipe below the powder feeder at an initial velocity of 0.5 m/s in the x-direction where they instantaneously experience a higher gas velocity just as in the test rig.

The DEM parameters for the particles, such as the particle size, particle density, surface energy, the P–P and P–W friction coefficient, were measured in the laboratory. Other parameters, i.e. the coefficient of restitution, the Poisson ratio and Young's modulus of elasticity, were obtained from DEM calibration simulations for the powder rheometer test and the angle of repose test in conjunction with experimental results from the same instruments. Table 7 shows a summary of the DEM parameters used for all coupled simulations.

The DEM parameters for the 316L stainless steel pipe, i.e. density, modulus of elasticity, and coefficient of friction were obtained from

Table 5
Summary of the simulation Conditions.

Simulation Parameter	Value
Method	*CFD-DEM*
Fluid velocity [m/s]	11.5, 16.5
Air density [kg/m^3]	1.225
Fluid viscosity [kg/m s]	1.789×10^{-5}
Turbulence model	Standard k- ε with enhanced wall treatment
Solution method	Coupled SIMPLE
Boundary Conditions	
Inlet	
Turbulent Intensity [%]	4.3
Hydraulic Diameter [m]	0.047
Outlet	
Turbulent Intensity [%]	4.3
Hydraulic Diameter [m]	0.047
Pressure outlet (gauge) [Pa]	0.0
Wall	
No-slip boundary [m/s]	0.0
F–P Interaction	
Drag model	Haider and Levenspiel
Lift model	Saffman and Magnus lift
P–P & P–W Interactions	
P–P & P–W Contact model	Non-linear Hertz-Mindlin with JKR
Time step selection	
Fluid flow time step [s]	2.5×10^{-5}
DEM Time step [s]	1.5×10^{-7}

the literature. The P–W interaction parameter, i.e. the P–W friction coefficient was estimated from wall friction tests in a FT4 powder rheometer. The surface energy of the particle was measured using the contact angle technique [44]. The P–W surface energy was estimated from the average of the individual surface energy of the particles (γ_p) and the stainless steel (γ_w) as suggested by Young's correlation as shwon in eq. (18) thus[45]:

$$\gamma_{p-w} = \gamma_p + \gamma_w - 2\sqrt{\gamma_p\gamma_w} \tag{18}$$

3.3.2. Time step selection

In the coupling between CFD and DEM it is presumed that during a time step of the fluid flow simulation only a single collision takes place and that the forces acting on any particle remain constant. This puts a severe restriction to the time step for the fluid flow simulation. The largest DEM time step allowed is set equal to the Rayleigh time (T_R), denoting the time taken for a shear wave to propagate across a particle [42]. It is given by:

$$T_R = \frac{\pi R\sqrt{\rho_p/G}}{(0.1631v + 0.8766)} \tag{19}$$

Eq. (19) shows the Rayleigh time step is inversely proportional to the square root of the shear modulus (G), implying that harder particles need a smaller time step. It is recommended to set the DEM time step to smaller than 20% of the Rayleigh time step [42]. In the current study, the time scales such as the time for particle to pass a control volume, the particle response time and the integral time scale of turbulence are all checked against Rayleigh time step, and the smallest time step is used. While T_R was estimated to be $1.75 \times 10^{-6}s$, the particle response time τ_p was estimated as 0.033s when using the particle properties in Table 6 and the fluid viscosity. The DEM time step was set to ~9% of T_R as shown in Table 6. As in the coupled CFD-DEM simulation the recommended time step for the Fluent simulations should be 100 times larger than the DEM time step, the fluid time step was reduced to $2.5 \times 10^{-5}s$ which is smaller than the fluid time step required from the Courant-Friedrich-Lewy (CFL) condition (being $6 \times 10^{-5}s$).

The coupled CFD-DEM simulation took a CPU time between 353 h (~2 weeks) to 853 h (a month) for the fastest run (R5) and the slowest (R2), respectively, on an Intel Xeon E5680 processor with 44 cores and 128 GB of RAM. The flow simulation time was 8s with first particles arriving at the exit after 2s. After 8s, the particles have achieved a statistically steady flow through the entire flow loop in all cases. The simulation data was recorded every 0.01s for post-processing.

3.3.3. Mesh independence study

Mesh size and quality affect convergence, duration and accuracy of any simulation including our CFD-DEM simulations. We therefore carried out a mesh sensitivity study for a gas flow only condition. The superficial gas velocity used in the test rig was set as a boundary condition at the inlet. With the aid of a pressure drop measurement for the test rig for a clear gas flow, a suitable mesh size was selected which results in reasonably accurate results and a moderately expensive computational time. Table 7 shows a summary of the grid independency study. Case IV seemed to be a good compromise between accuracy of the pressure drop prediction and computational time needed; hence, this mesh size was selected. It is considerably larger than particle size and substantially smaller than the system dimensions.

Table 6
DEM Parameters for the cohesive FFMP particles and stainless-steel pipe.

DEM Properties Parameters	Value
Fat-Filled Milk Powder (FFMP) Properties	
Particle Density [kg/m^3]	1187
Particle Feed rate [g/s]	0.5, 1.1
Poisson Ratio [−]	0.25
Average Particle Size [μm]	93.5
Coefficient of Restitution (*P–P*)	0.54
Coefficient of Friction (*P–P*)	0.33
Shear Modulus (Pa)	1×10^7
Sphericity (∅)	0.565
P–P Surface Energy - γ_p (mJ/m^2)	160.9
Wall Properties (Stainless Steel Pipe)	
Material Density [kg/m^3]	7580.0
Poisson Ratio (*P–W*)	0.30
Coefficient of Restitution (*P–W*)	0.5
Coefficient of Friction (*P–W*)	0.43
Shear Modulus (Pa)	1×10^{10}
Wall Surface Energy- γ_w [mJ/m^2]	42.43
P–W Surface Energy γ_{p-w} [mJ/m^2]	38.08

3.3.4. Powder properties and DEM parameters calibration

The DEM simulation requires a good calibration of the cohesive dairy powder properties to predict correctly the flow behaviour. A set of DEM parameters were tested in a horizontal pipe using the measured physical properties of the FFMP fines (Table 1) and the calibrated DEM parameters for the FFMP fines shown in Table 6. Fig. 6(a) and Fig. 6(b) illustrate the significance of using correct powder properties in deriving the P–P and P–W interaction parameters (such as the surface energy, the friction coefficient, particle shape and sizes).

Fig. 6(a) shows the effect of an erroneous prediction of the contact between the cohesive powders and the stainless-steel pipe due to an inaccurate estimation of the P–W surface energy parameter, γ_{p-w}. The γ_{p-w} was first assumed to be equal to the P–P surface energy (i.e. 160 mJ/m^2). The particles were observed bouncing back upwards to a substantial degree, against gravity (see Fig. 6 (a)), due to an overestimation of the repelling force during collisions with the wall. In contrast, Fig. 6 (b) shows a more accurate result, obtained by now using the calibrated DEM parameters and the Young's correlation in eq. (19) for the γ_{p-w} surface energy (i.e. 38 mJ/m^2).

4. Results and discussion

Four experiments were performed in duplicate to collect various data (particle volume fraction, pressure drop, deposition) with respect to the effect of two major parameters on fine powder transport. The conveying gas velocities were in the range 11–17 m/s while the fines loading ratios amounted to 0.015 and 0.045 (see Table 4). In addition, four cases similar to these four sets of experiments were simulated by means of ANSYS Fluent/EDEM coupling. Comparing the computational with the experimental results may increase confidence in such CFD-DEM modelling of conveying cohesive (dairy) particles. While the experimental data may have been collected under steady-state conditions, the computational runs only covered a short period of time (of the order of 8 s only) sufficient to let particles reach the exit of the pipe system but insufficient for reaching a statistically steady-state.

4.1. Particle behaviour and peak volume fractions

Table 8 presents experimental values and CFD-DEM simulation results for the peaks of the PDFs of the local particle volume fractions at

Table 7
Grid parameters and Pressure Drop.

Parameters	Case I	Case II	Case III	Case IV	Case V	Exp.
Mesh Element size (m)	0.012	0.010	0.0060	0.004	0.002	–
Number of Elements	10,712	14,210	52,544	149,544	1,099,085	–
Pressure Drop (Pa)	135.3	137.5	123.5	156.7	157.8	160.5

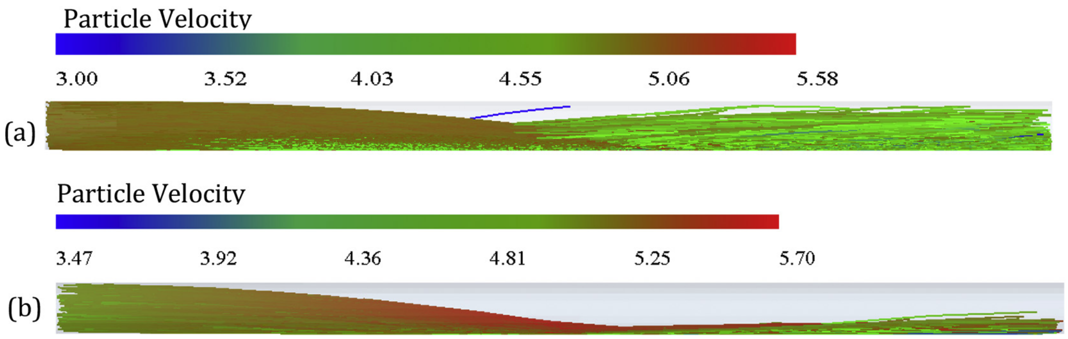

Fig. 6. Streamlines of particle trajectory of (a) non-calibrated (b) calibrated cohesive CFD-DEM simulation of pneumatic conveying of dairy powder in a horizontal pipe.

Table 8
Local peak of the PDF of particle volume fraction.

RUNS		Vertical Probe (%)	Horizontal Probes (%)		Powder Deposition (wt. %)
		V1	H1	H2	
R1	Experiment	0.648	0.018	0.016	6.41
R3	Experiment	0.631	0.017	0.015	6.58
	Simulation	0.651	0.022	0.021	–
R2	Experiment	0.966	0.032	0.026	9.33
R6	Experiment	0.954	0.029	0.025	9.62
	Simulation	0.968	0.034	0.028	–
R5	Experiment	0.370	0.258	0.210	4.92
R4	Experiment	0.363	0.249	0.203	5.11
	Simulation	0.373	0.265	0.223	–
R7	Experiment	0.861	0.482	0.397	6.34
R8	Experiment	0.847	0.464	0.383	6.45
	Simulation	0.843	0.507	0.404	–

the three locations. Several observations can be made on this Table, both qualitatively and quantitatively:

- First of all, experimental and simulated data are rather similar: the discrepancies for V1 are 2% or less, while H1 and H2 discrepancies vary between 2% and (for R1) 30%. These similarities are indicative of a substantial degree of quantitative correctness and of a considerable reliability of the CFD-DEM simulations.
- Then, in each case, peak volume fraction values at V1 are substantially higher than those at H1 and H2, indicating that the gas flow struggles with overcoming gravity such that particles tend to collect in the vertical pipe, resulting in mutual collisions, agglomeration into clumps, and deposition on the pipe wall.
- This effect decreases at higher gas flow rates (V1 values in R1 are higher than in R5, and V1 values in R2 are higher than in R7) such that H1 and H2 values are higher by at least an order of magnitude.
- As expected, V1 values at high solids loading exceed those at low solids loading.
- Values at H2 are always lower than those at H1 which is due to particles depositing underway; this effect increases with increasing solids loading.
- In the experiments, particle deposition (most right column of Table 8) increases with increasing solids loading and decreases with increasing gas flow rate.

Many conclusions from the quantitative data of Table 8 are supported by snapshots taken from the simulations as presented in Figs. 7 and 8. For runs R1 and R2, at low gas flow rates, Fig. 7(a) and (b) show many agglomerates, clumps and clusters of varying size in the vertical pipe, with low or (almost) zero velocity and/or deposited on the pipe wall, while Fig. 8(a) and (b) show higher particles concentrations approaching the V–H bend and particles just succeeding in passing the bend while staying close to the 'bottom' of the horizontal pipe section. In runs R5 and R7 – see Fig. 7(c), (d), 8(c) and 8(d) – the higher gas velocity largely outclassing gravity, particles including some clusters mostly travel upwards along the 'right-hand side' of the vertical pipe (as a result of taking the outside bend in the upstream H–V bend), take again the outside V–H bend (again due to their inertia derived from the higher gas velocity) and then drop out collectively in a nice curve to the 'bottom' of the horizontal section.

Figs. 9–12 illustrate for each of the four runs R1, R2, R5, and R7 the dynamic variations of the local volume fraction at the three test rig locations V1, H1 and H2 in terms of time traces and probability distributions (PDFs), both measured and simulated. Note that in these

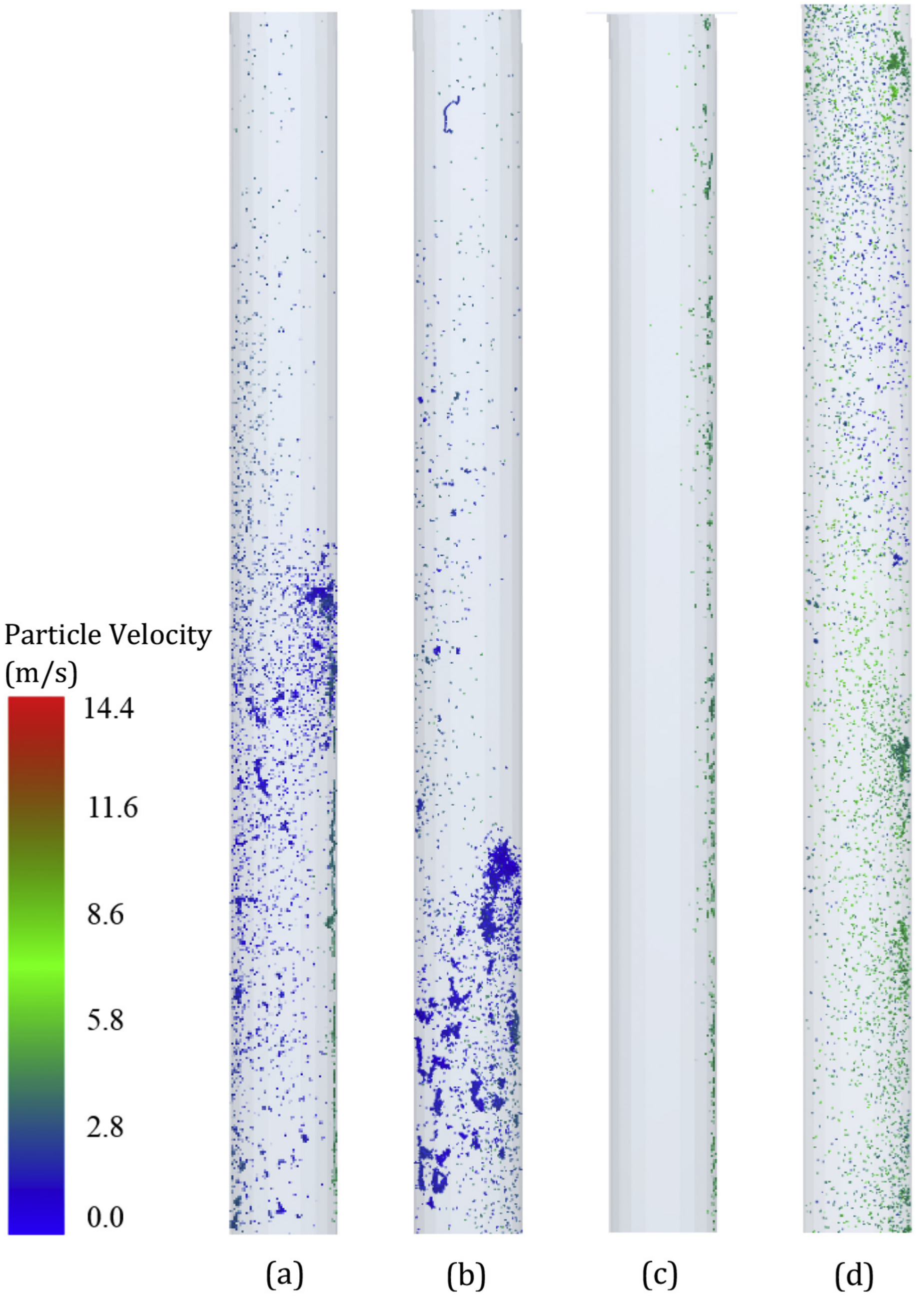

Fig. 7. Particle deposition on the vertical pipe coloured by particle velocity for (a) R1, (b) R2, (c) R5, and (d) R7, all after 3.0 s of simulation.

figures the scales are not identical everywhere, due to the large variations in operating conditions and due to the different probe locations. Given that the simulations are not really steady-state yet, the general conclusion from comparing the experimental data and the computational results in these figures is that the CFD-DEM approach is a rather good predictor for the gas-solids transport in a pipeline system with H–V and V–H bends. This applies to both the time traces and the PDFs.

Fig. 9(a)–9(c) relate to R1. The time traces show strong fluctuations in volume fraction as a result of intermittent accelerations and decelerations of particle clumps. This may be due to the low gas velocity, which may not be capable of re-accelerating the particles after they have passed the H–V bend. As a result, many of the particles do not make it up to the next bend and start hanging around in the vertical pipe section. They experience strong P–P and P–W interactions, get agglomerated, form clumps such that vertical transport and dispersion even get harder, and deposit and stick onto the pipe walls. This was also concluded from Fig. 8. Substantially fewer particles pass the V–H bend and the probes H1 and H2 as shown in Fig. 9(b) and (c), respectively. The particle volume fractions of the two horizontal probes were within a fairly narrow interval as shown in Fig. 9(b) and (c). The peak of the volume fraction distribution at H2 is 40 times smaller than that at V1. In contrast, it is only 1.2 times smaller than at H1.

Fig. 10(a)–10(c) present time traces and PDFs for R2 with a higher mass loading at the same low gas velocity showing similar trends as for R1. The higher mass loading makes it harder for the gas to accelerate all particles supplied via the H–V bend all the way up to the next bend; this results in more frequent collisions in the vertical section, stronger agglomeration and more deposition/sticking onto the pipe wall. This is demonstrated by the wider span of the measured volume fraction in Fig. 10(a) compared to Fig. 9(a). The ratio of the peak of the PDFs of the measured volume fractions at V1 and H2 amounts to 37, while the H1 and H2

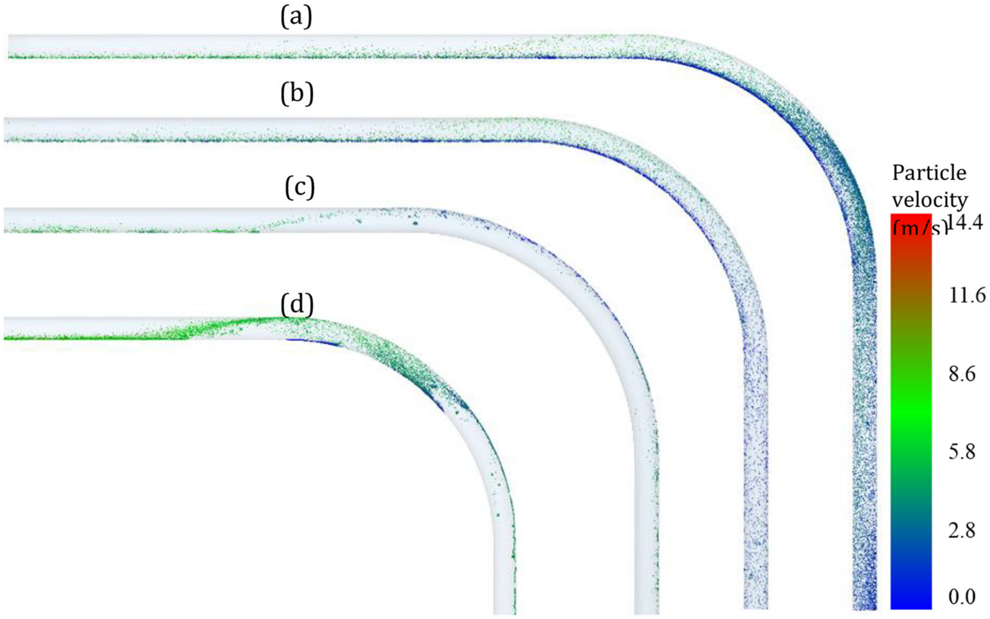

Fig. 8. Particle Deposition on the downstream horizontal pipe after the H–V and V–H Bends for (a) R1, (b) R2, (c) R5, and (d) R7, all after 8.0 s of simulation.

probes differ by a factor of 1.23 – values which are similar to those in R1.

At higher gas velocity, see Fig. 11(a)–11(c) and Fig. 12(a)–12(c) for R5 (low solid feed rate) and for R7 (higher solid feed rate), respectively, the fluid-particle interaction forces are better able to overcome the P–P and P–W interaction forces, and the particles in the vertical pipe section are much more easily re-accelerated and find much more easily their way via the V–H bend into the horizontal pipe section. Also, the ratio of the peaks of the PDFs of the measured volume fraction at V1 and H2 reduces to just 1.8 (in R5) and 2.2 (in R7), while the peak probe values at H1 and H2 again differ by only 1.23 and 1.21, respectively: equal to the values in R1 and R2. The remarkable difference in the ratios of the peak values at V1 and H2 found for different gas velocities at similar solids loading (R1 and R5) reflects that the conveying capacity of a pipeline system is very strongly dependent on the gas flow rate and to a much lesser degree on the solids loading.

4.2. Pressure drop

For the four cases considered, the simulated pressure drop was consistently lower than the experimentally measured pressure drop, as shown in Table 9. The discrepancy is in the order of 5–10%, may be mainly due to a different configuration at the inlet of the pipe system: while in the experiment the gas was supplied via a narrow inlet pipe. In the simulation the inlet condition was a uniform gas velocity. However, pressure drop increases with increasing solids loading at constant velocity or with increasing gas velocity at constant solids loadings. Pressure drop can be correlated with particle deposition as measured in the experiment as shown in Table 8 in section 4.1. Increasing the gas flow rate such that the pressure drop doubles (from 237.5 Pa to 453.3 Pa), at the low solids loading (as in R1/R3 and R5/R4), reduces particle deposition from 6.4 to 4.9 wt%. Similarly, for the high solids loading, gas velocity in R7 being higher than in R2 decreased the particle deposition from 9.3 to 6.3 wt%. These data once more illustrate and quantify the effect of gas flow rate on particle deposition.

4.3. Particle-wall deposition

Different deposition patterns are observed in the various pipe bends, both in the experiments (pictures were taken after the completion of the experiment) and in the simulation. Overall, experimental and simulated deposition patterns in each of the bends qualitatively agree very well.

At low gas velocity, as in R2 and R1, the P–P cohesive and the P–W adhesive forces dominate over the F–P drag force and the pressure gradient force. This leads to increases in inter-particle re-agglomeration and P–W deposition. This effect is more severe in the pipe bends, and downstream of bends due to the centrifugal effect and the resulting secondary flow (roping). Fig. 13(a) and (b) show particle deposition on the inner-wall of the H–V bend both in R1 (low solids loading) and R2 (higher solids loading). With the low solids loading, part of the powder deposited on the bend are re-entrained in the downstream vertical pipe – see Fig. 7(a) – and this results in lower build-up of deposits at this bend, as shown in Fig. 13(a). At higher solids loading, however, the deposited particles are rarely re-suspended in the vertical pipe, as shown in Fig. 7(b), thereby leading to increase in the build-up of powders at this bend section, as shown in Fig. 13(b).

In the V–H bend (Fig. 14), effects of gravity, P–W adhesion and secondary flow phenomena upstream play a major role. At low gas velocity and low solids loading (R1), these effects hinder the re-acceleration of particles, resulting in particles depositing on the bottom of the inner side of the bend as well as downstream of the bend, as shown in Figs. 14(a) and 8(a) respectively. At higher solids loading (R2), the re-acceleration in the vertical pipe is slower and hence results in an increase of the powder build-up at this bends and on the downstream of this bend, as shown in Figs. 14(b) and 8(b).

At higher gas velocity (R5 and R7), the F–P drag force and the pressure gradient force minimise the effect of the gravitational force, the P–P cohesive force, and the P–W adhesive force. This accounts for even re-agglomerated fines staying suspended in the flow with no significant deposition in R5 as shown by Figs. 13(c), 14(c) and 7(c), and 8(c) for the H–V bend, the V–H bend, the

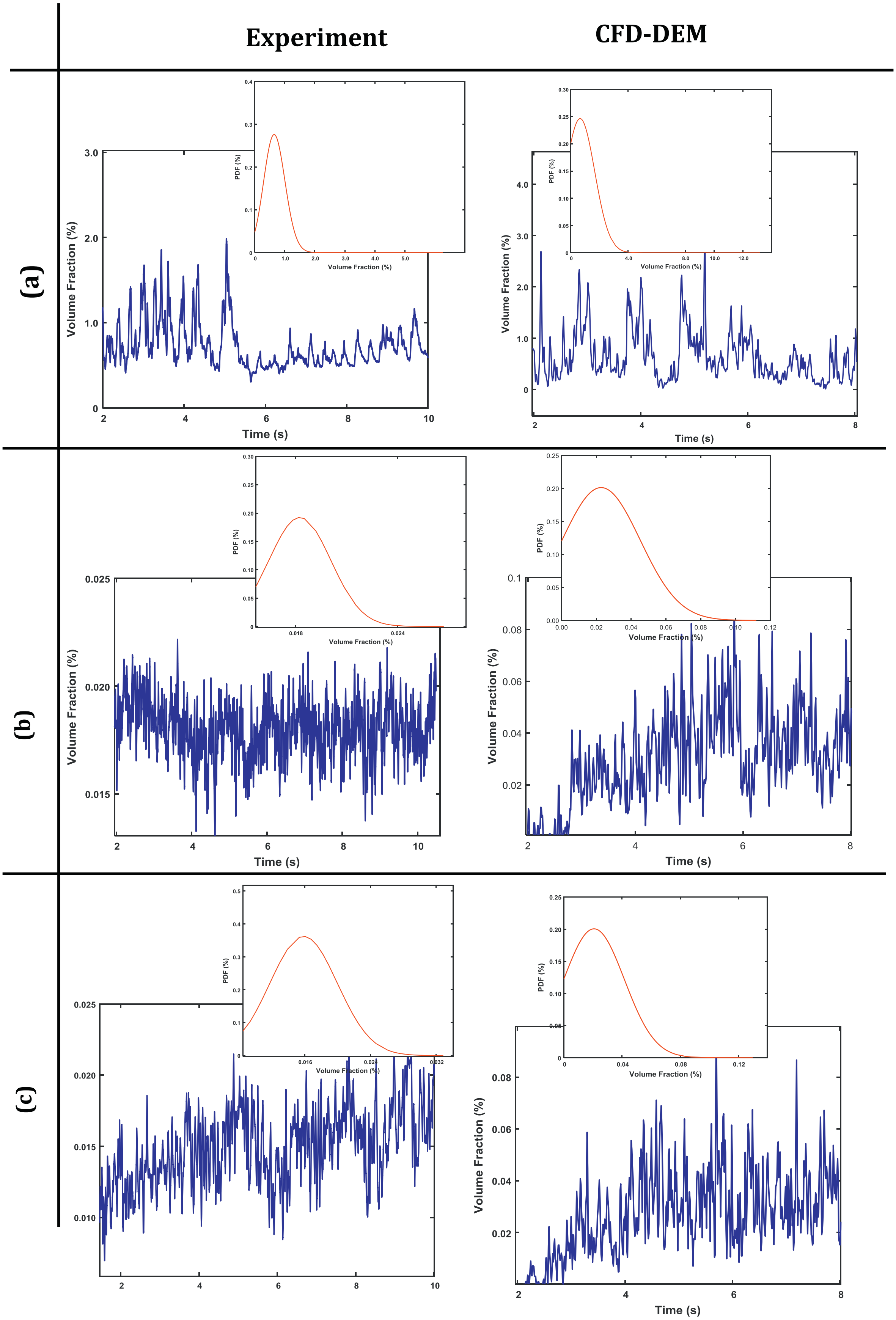

Fig. 9. Comparison between experiment and CFD-DEM results for R1 at location(a) V1,(b) H1, and(C) H2.

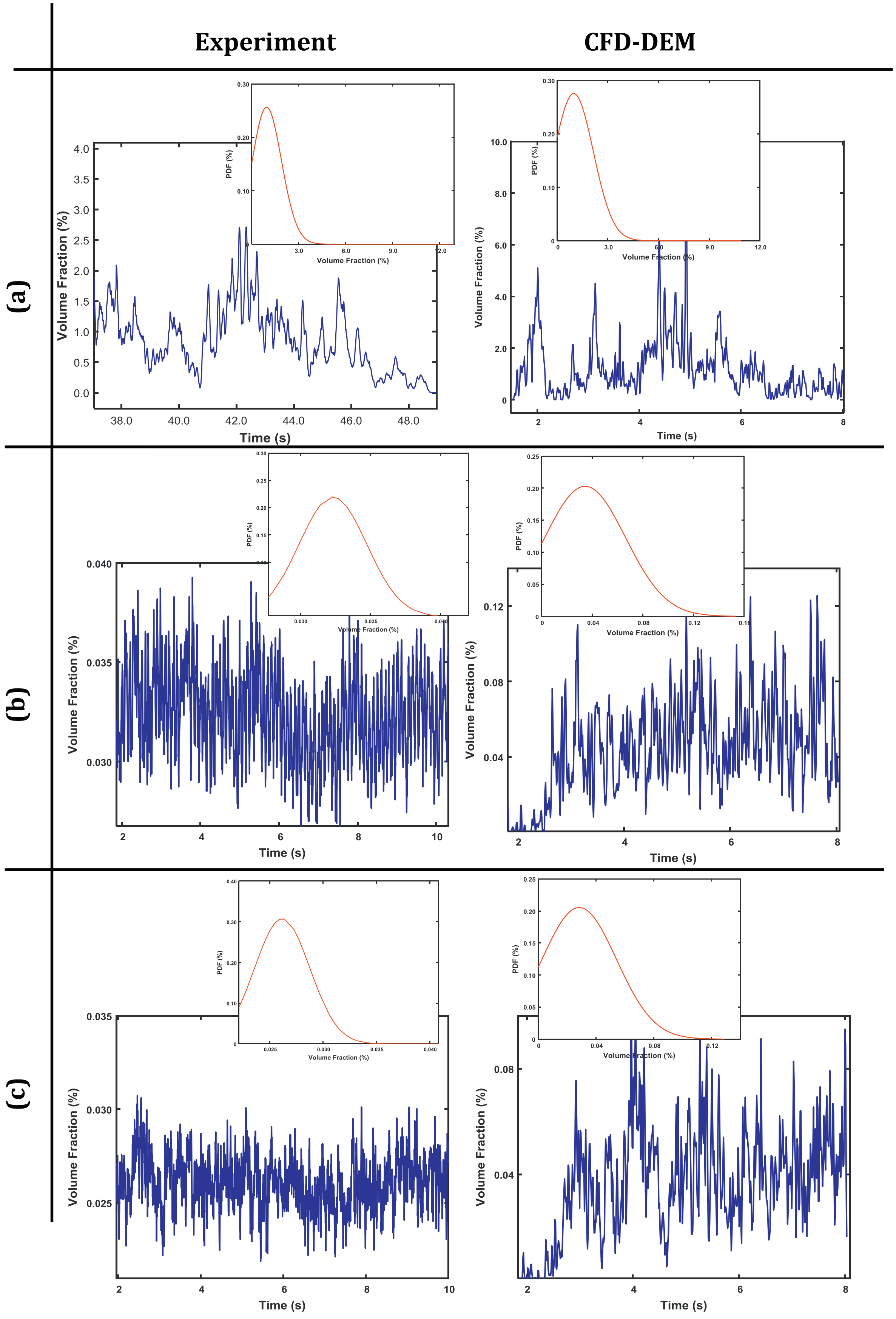

Fig. 10. Comparison between experiment and CFD-DEM results for R2 at location(a) V1, (b) H1, and (c) H2.

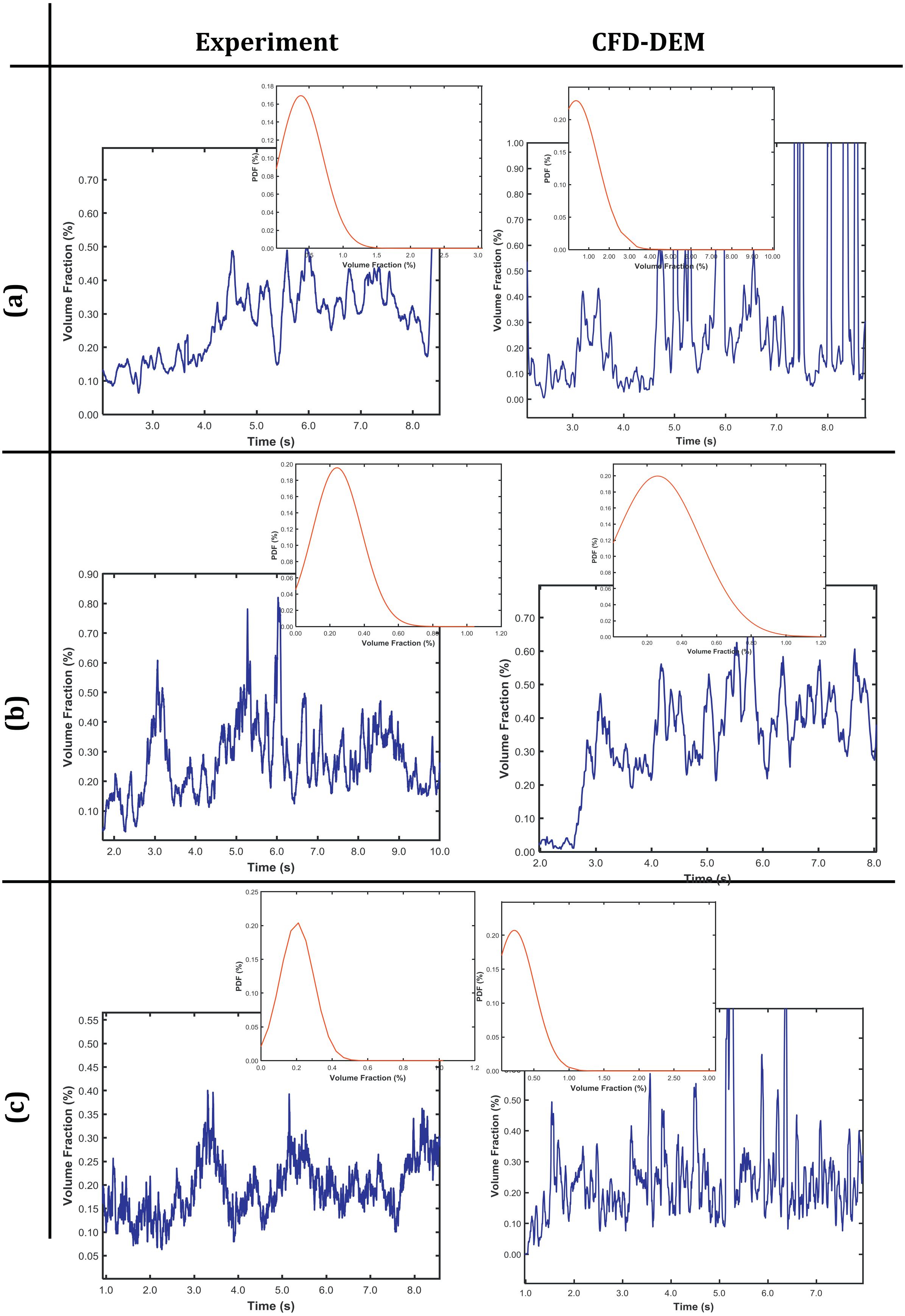

Fig. 11. Comparison between experiment and CFD-DEM results for R5 at location(a) V1,(b) H1, and(c) H2.

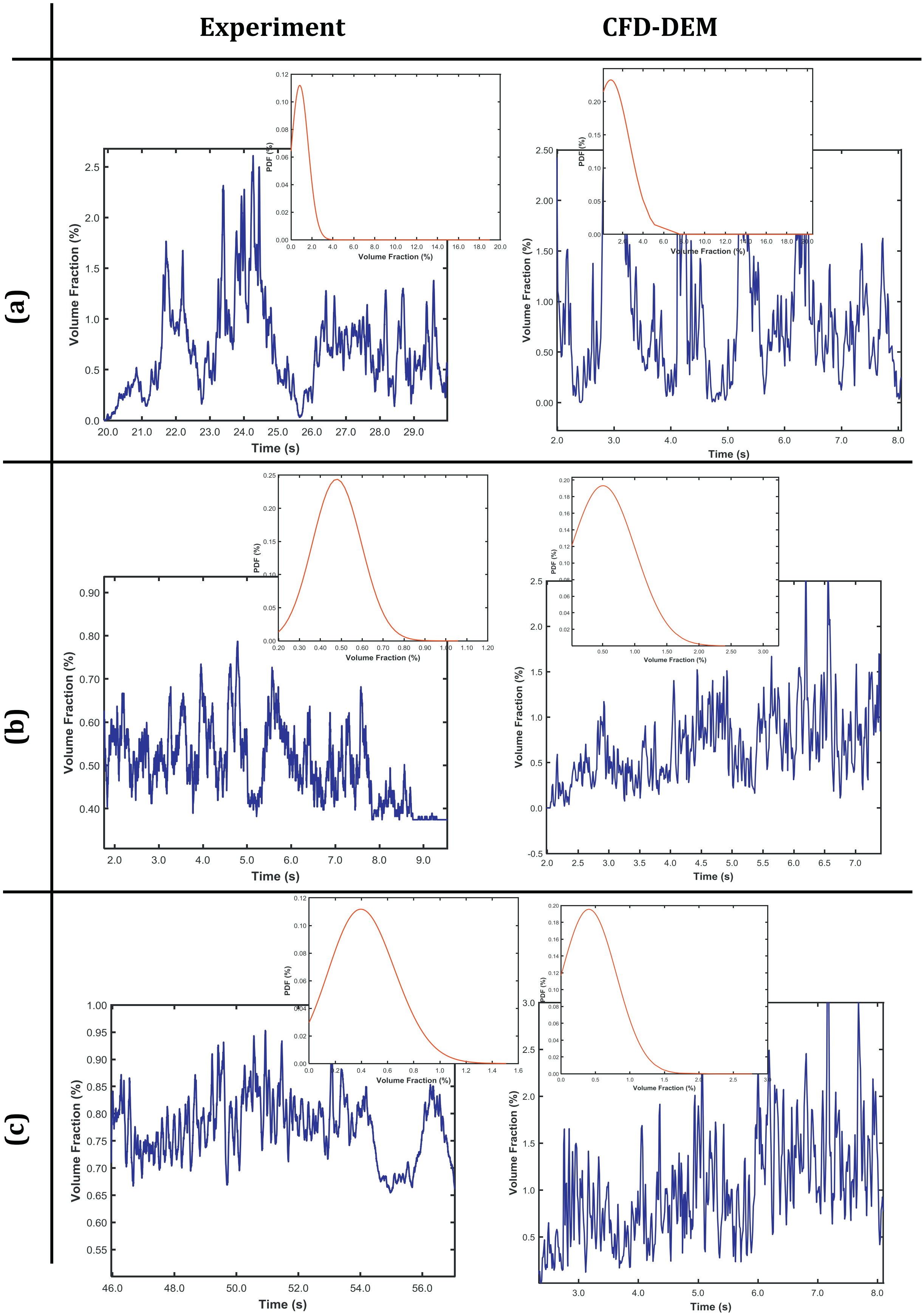

Fig. 12. Comparison between experiment and CFD-DEM results for R7 at location(a) V1,(b) H1, and(c) H2.

Table 9
Pressure drop in the conveying system.

RUNS	Feed rate [g/s]	Gas velocity [m/s]	Pressure drop (Gas only) [Pa]	Pressure drop (with solid flow) Experiment [Pa]	Pressure drop (with solid flow) CFD-DEM [Pa]
R1	0.5	11.5	160.5	218.5	237.5
R3				225.1	
R2	1.1	11.5	160.5	268.3	285.7
R6				272.4	
R5	0.5	16.5	359.8	429.7	453.3
R4				440.2	
R7	1.1	16.5	359.8	493.1	512.4
R8				501.6	

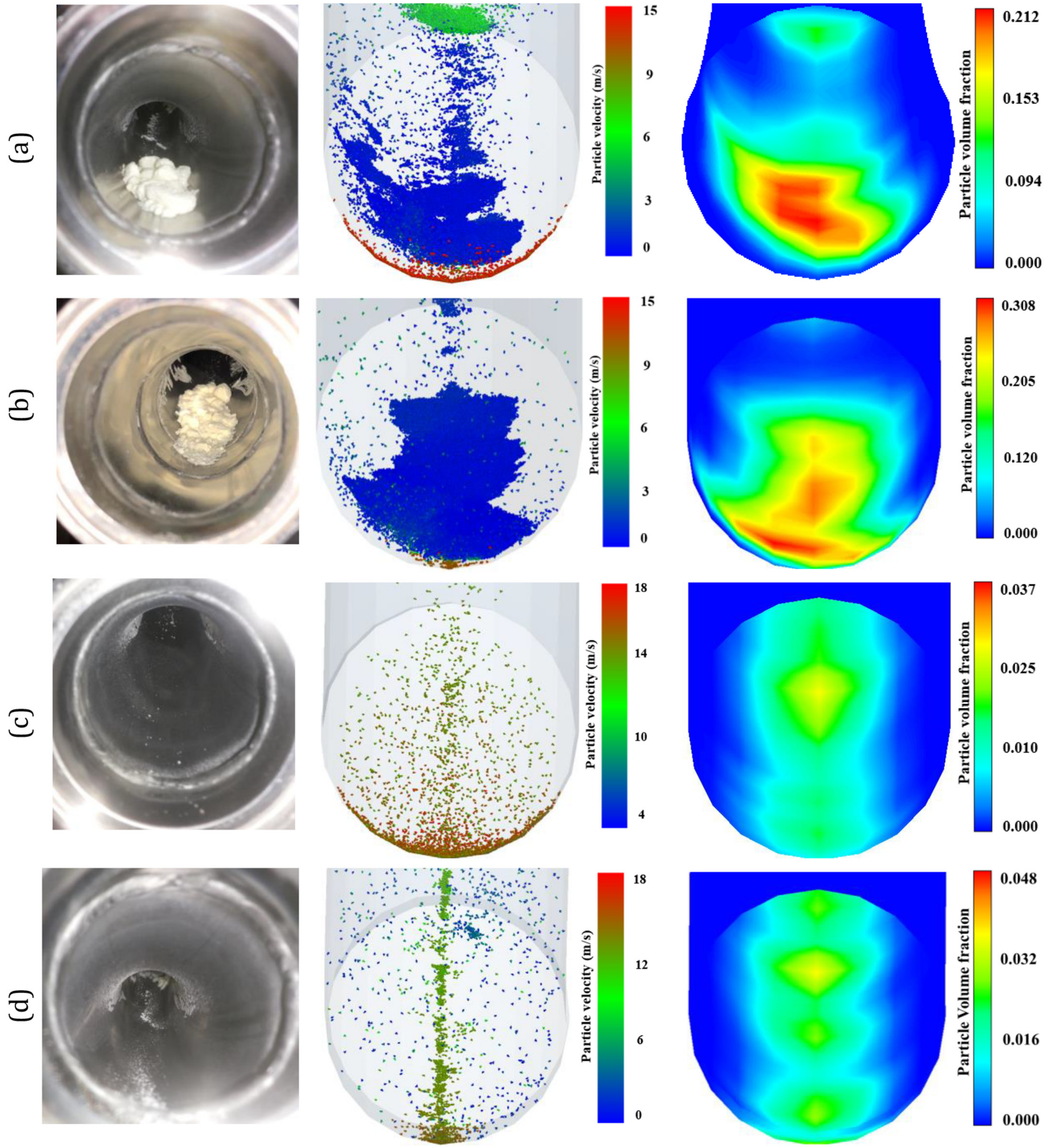

Fig. 13. Comparison of CFD-DEM simulated flow patterns of particle deposition with experiments on the inner-wall of the H–V pipe bend for (a) R1, (b) R2, (c) R5, and (d) R7.

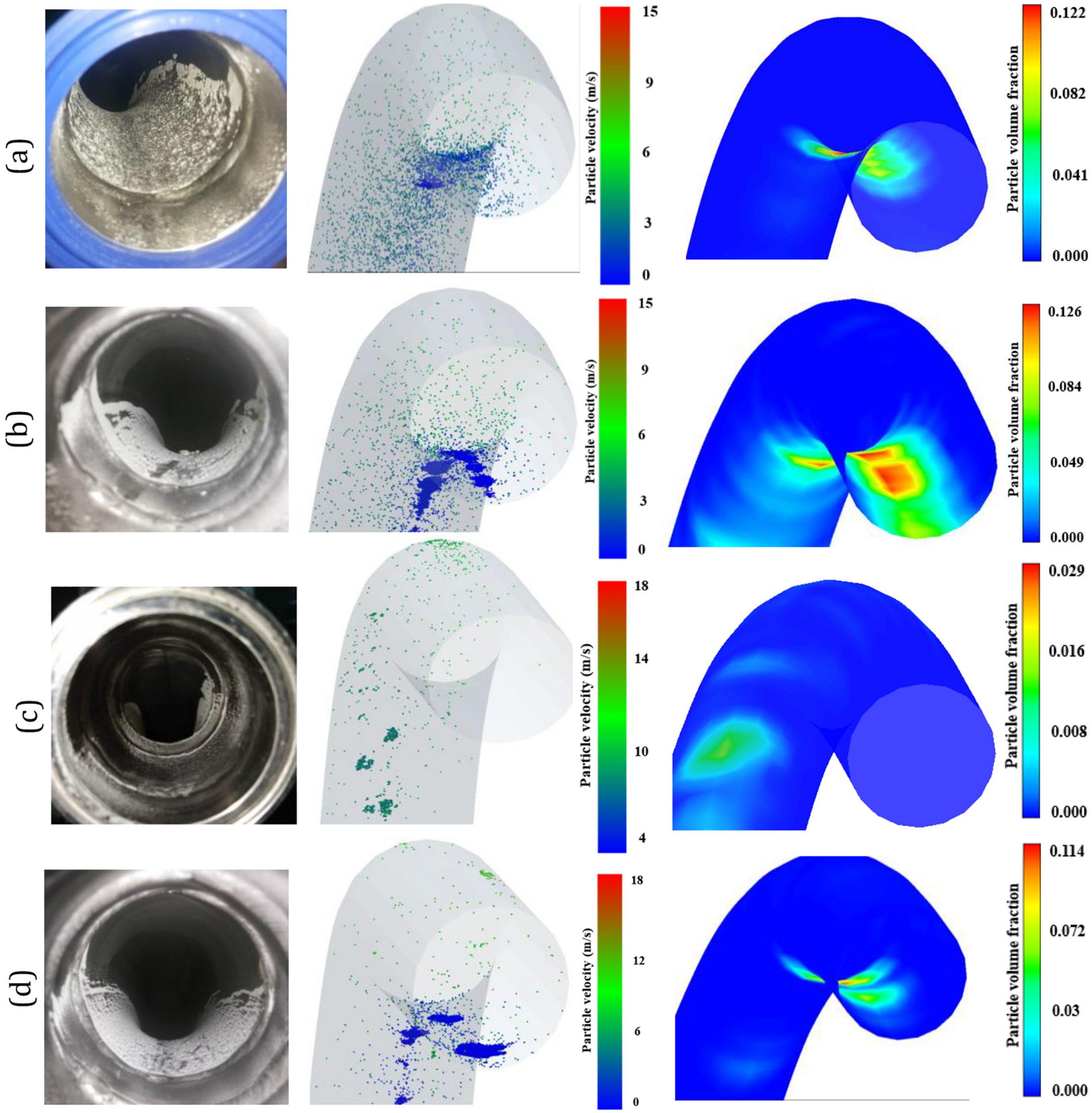

Fig. 14. Comparison of CFD-DEM simulated flow patterns of particle deposition with Experiments on the inner-wall of the V–H pipe bends for (a) R1 (b) R2 (c) R5, and (d) R7.

downstream vertical and the downstream horizontal pipes, respectively. As the solid flow rate is increased at the same gas velocity (R7), Fig. 13(d) illustrates how some particles collect on the pipe bottom in the H–V bend which are re-suspended again and dispersed rapidly in the vertical pipe as shown in Fig. 13(d). In the V–H bend, an increase in the build-up of powders is then observed due to the increase in solid deceleration at the high solids loading and due to the secondary flow effect, as illustrated in Fig. 14(d). This results in a comparatively lower re-entrainment of deposited powders downstream of the V–H bend, as shown in Fig. 8(d).

A more complex flow structure is observed in the H–H bend in all cases analysed. Generally, all the four cases show varying degrees of particle deposition on the inner-wall of the H–H bends both in the experimental study and in the CFD-DEM simulation, as shown in Fig. 15(a) to Fig. 15(d). Particle ropes formed in the H–H bend due to the secondary flow do not disperse directly (compared to H–V and the V–H bends) but keep moving along with a spiral form around the outer and inner-wall of the bend, as can be clearly seen in the experimental snapshots and the simulated cases of Fig. 15(a) and (b) for R1 and R2, respectively. The particles keep close to the inner-wall when they exit from the bend section. At the higher gas velocity and lower solids loading (R5), only a minimum amount of powder deposits can be seen in the H–H bend - see in Fig. 15(c) both experiment and simulation. For increasing

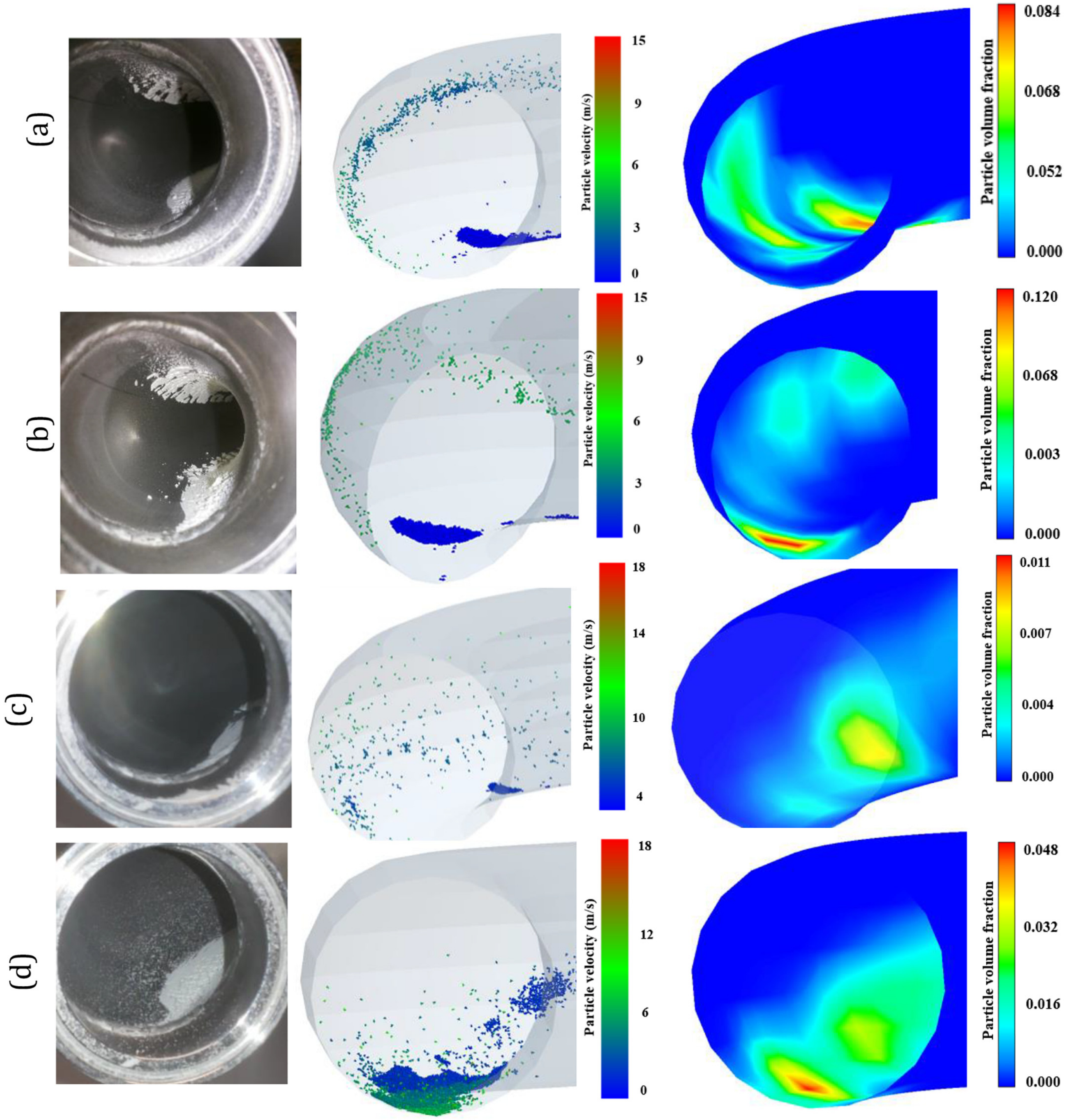

Fig. 15. Comparison of CFD-DEM simulated flow patterns of particle deposition with Experiments on the inner-wall of the H–H pipe bend for (a) R1, (b) R2, (c) R5, and (d) R7.

solids loading and decreasing gas velocity, deposition increases as demonstrated by Fig. 15(d), (b) and 15(a).

5. Conclusions

In this study, we perform an experimental and numerical study on pneumatic conveying of cohesive dairy powder. The idea was to develop a computational approach making conveying experiments redundant. The experiments served to validate the computational approach making use of a CFD-DEM software tool (ANSYS Fluent/EDEM). The study was about assessing how different operating conditions influence the dynamics of dilute cohesive dairy powder flow.

A novel element in the experimental study is the use of an optical technique for measuring the dynamics of local particle volume fraction (time traces and probability density functions) as a function of air velocity and solids loading. In addition, pressure drop, and powder deposition were measured for several operating conditions. The simulation technique was used to produce the data by computation.

The main findings are summarised as follows:

- We convincingly demonstrated that the dilute phase conveying of cohesive dairy powder is dominated by particle-particle and particle-wall interactions (collision and wall adhesion).
- Including the lift forces in the calculations makes a 20% difference in the fluid-particle interaction force overall.
- The local peak values of the PDFs of particle volume fraction from the CFD-DEM simulations are in close agreement with experimental data. The discrepancies between experimental and simulation results are within 2% or less for the vertical probes, V1, for all cases. For the horizontal probes, H1 and H2, the absolute errors in the peak value of the PDFs amounted to some 30% for run R1 and about 2% for all other cases. The PDFs are a fingerprint of the dynamics of the gas-solids flow.
- In terms of the pressure drop, the simulations correctly predict the effects of increasing gas flow rate and solids loading on the pressure drop. The discrepancy between the experimental and simulation data is within ±5% to ±10% for all cases. Pressure drop increases with increasing air velocity at constant solids loading or with increasing solids loading at constant air velocity. The sensitivity for gas velocity turns out to be higher.
- The particle deposition measured in the experiment correlates well with the experimental pressure drop. Increasing the gas flow rate such that the pressure drop doubles, at low solid loading, reduces particle deposition by ~1.5 wt%. Also, increasing the gas velocity, at high solid loading reduces particle deposition by ~3 wt %.
- The deposition patterns in the H–V, the V–H and the H–H bend sections in the experiments agree with the flow patterns in the CFD-DEM simulations. In the H–V bend, a large build-up of particle is observed at high solids loading, while it is lower at lower solids loading. In the V–H bend, however, a comparatively smaller powder build-up is observed, with more settling on the downstream horizontal pipe than in the bend. In the H–H bend, a more complex flow pattern develops with varying degrees of particle deposition at the inner walls of the bend.

Based on the strong agreement between experimental and computational results, we conclude that the CFD-DEM simulations may safely be used for exploring conditions and means for reducing particle deposition (and blockage) in cohesive (dairy) powder transport. The CFD-DEM technique does require substantial computational time and computing resources. A future study will investigate the effect of the conveying configurations (i.e. the size, types and amount of bends) on the flow characteristics of cohesive powders during conveying. Further studies on the quantitative effects of wall boundary conditions and turbulence modulation (beyond the scope of the current study) with respect to particle clustering and flow steadiness may assist in further improving simulation of the conveying characteristics of cohesive dairy powder.

Acknowledgement

The authors acknowledge the Dairy Processing Technology Centre (DPTC), an Enterprise Ireland initiative; and the Technology Innovation Development Award (TIDA), a Science Foundation Ireland (SFI) initiative. The work was supported financially by the Irish State through funding from the Technology Centres Programme (Grant Agreement Number: TC/2014/0016) and the Science Foundation Ireland (Grant Agreement Number: 18/TIDA/5882).

Nomenclature

Symbols Units

a	contact radius m
A	contact area m^2
A_s	model constant
C_D	drag coefficient
E^*	effective modulus of elasticity Pa
$\boldsymbol{F}^c$	contact force N
$\boldsymbol{F}^f$	fluid-particle interaction force N
$F_{F-P,i}$	drag and lift force N
$\boldsymbol{F}^g$	gravitational force N
F_{JKR}	JKR normal force N
$\boldsymbol{F}^{nc}$	non-contact force N
G^*	effective shear modulus Pa
G_{solid}	powder feed rate kg/s
I	intensity of light with solid V
I_o	intensity of light with no solid V
$\boldsymbol{I_i}$	moment of inertia kgm^2
k	turbulence kinetic energy J/kg
K	cohesion energy density J/m^3
L_H	length of horizontal pipes m
L_V	length of vertical pipes m
m_i	mass of particle kg
n_m	number of particles
R_B	radius of bends m
R^*	effective particle radius m
Re_{sph}	particle Reynolds number
Re_Ω	rotational particle Reynolds number
$\boldsymbol{S}$	the volumetric force in each mesh cell N/m^3
S_t	tangential stiffness N/m
T_R	Rayleigh time step s
T_t	fluid time step s
$\boldsymbol{u}$	gas velocity vector m/s
$\boldsymbol{v}$	particle velocity vector m/s
$\boldsymbol{v}_i$	translational velocity of particle m/s
V_{air}	air velocity m/s
ΔV_{mesh}	computational cell volume m^3

Greek letters

γ	surface energy J/m^2
γ_p	surface energy of the particles J/m^2
γ_w	surface energy of the stainless steel J/m^2
δ_n	normal overlap m
δ_t	tangential overlap m
ε	turbulent dissipation rate m^2/s^3
μ	dynamic viscosity kg/(m.s)
ρ	fluid density kg/m^3
τ	the fluid viscous stress tensor Pa
τ_p	particle response time s
$\varnothing$	Corey shape factor
ϕ	volume fraction of FFMP
ϕ_{max}	volume fraction when pipe filled with FFMP
ω_i	rotational velocity rad/s

Abbreviations

CFD	computational fluid dynamics
DAQ	data acquisition unit
DEM	discrete element method
DNS	direct numerical simulation
DOE	design of experiment
ECT	electrical capacitance tomography
F– P	fluid-particle
FFMP	fat-filled milk powder
FOM	fibre-optical measurement
F–P	fluid-particle
H–H	horizontal-to-horizontal
H–V	horizontal-to-vertical
LB	lattice Boltzmann
LDA	laser doppler anemometry
LES	large eddy simulation
MDS	molecular dynamic simulation

PDA	phase doppler anemometry
PDF	probability density function
PIV	particle image velocimetry
P–P	particle-particle
PPM	pseudo-particle method
P–W	particle-wall
RANS	Reynolds averaged Naiver Stokes
V–H	vertical-to-horizontal

Appendix A

Fig. A1 for case R1 shows the individual P–P, P–W, and F–P forces (average of the magnitude of the force on each particle) in the domain evaluated at every time step. It can be seen from the figure that the P–W interaction dominates overall, higher than the P–P and F–P interaction by an order of magnitude and two orders of magnitude, respectively. This confirms the importance of the P-W forces in a dilute system with cohesive particles. Fig. A2 for case R7 shows a similar trend for the interaction forces. However, within the first 0.1s, the F–P forces were higher than the P–P forces. The higher gas velocity in case R7 means particle are accelerated more, and therefore the F–P are higher at the beginning of the simulation.

The effect of including the lift force in the F–P interaction was quantified based on the same cases (R1 and R7) as shown in Fig. A3. shows a qualitative comparison of "lift" and "no lift" effect on particle trajectories in the horizontal pipe. In the lift case, the number of particles in the upper section of the horizontal pipe increased compared to the "no

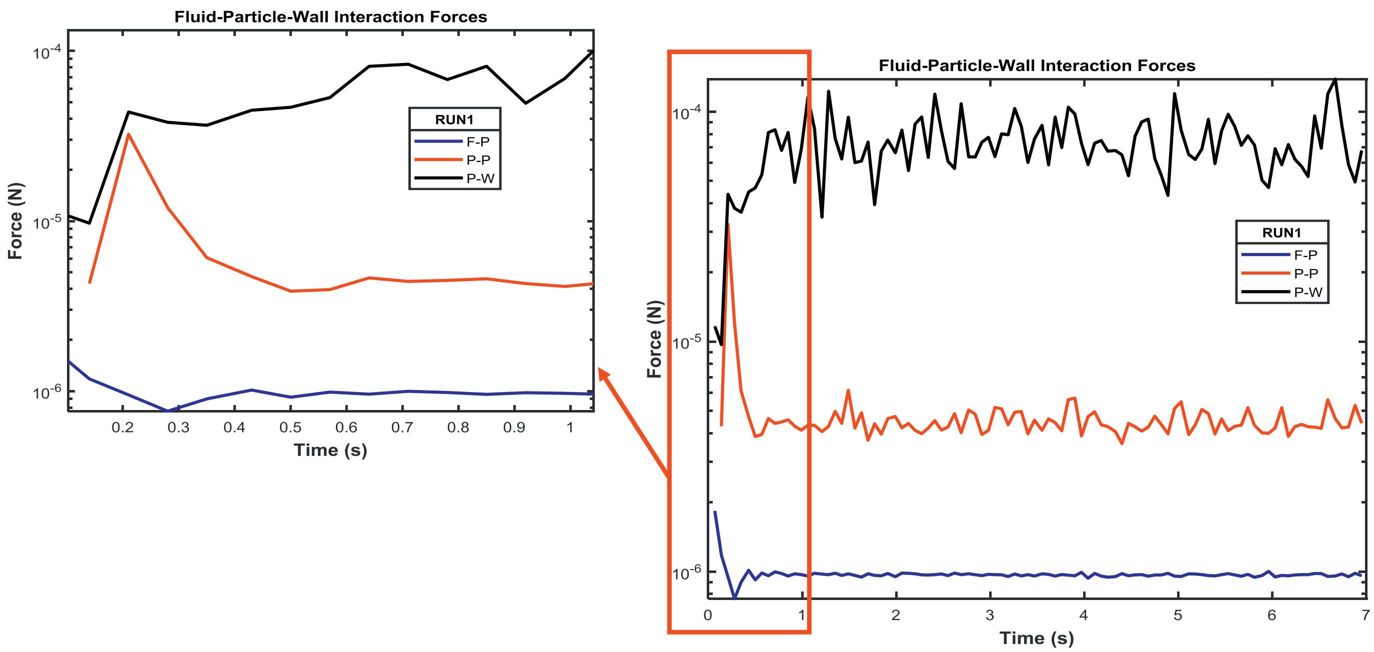

Fig. A1. Contribution of P–P, P–W and F–P interaction forces in case R1.

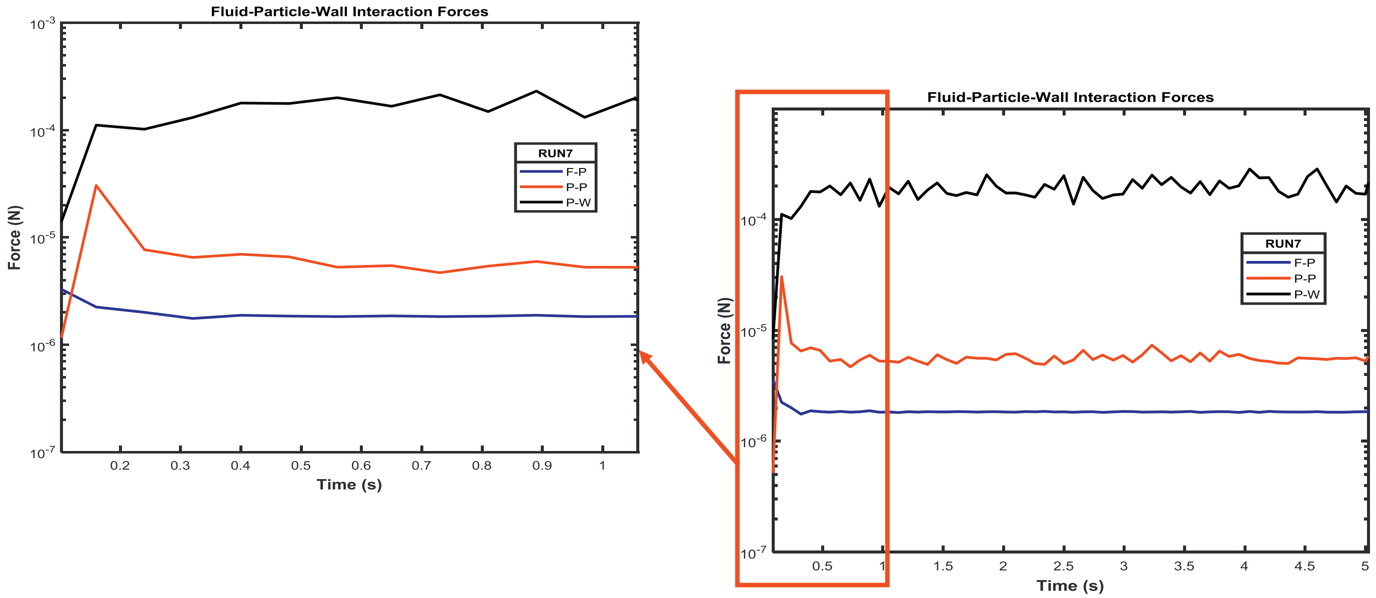

Fig. A2. Contribution of P–P, P–W and F–P interaction forces in R7 (plotted on a log scale).

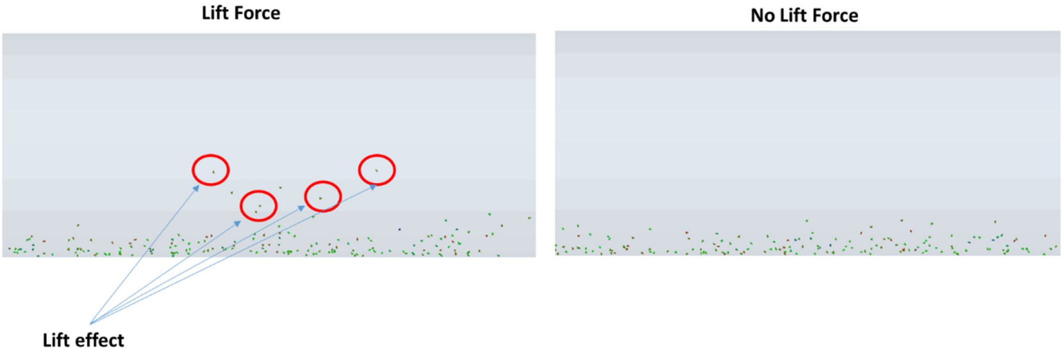

Fig. A3. Effect of lift force on particle trajectories in the horizontal pipe (R1).

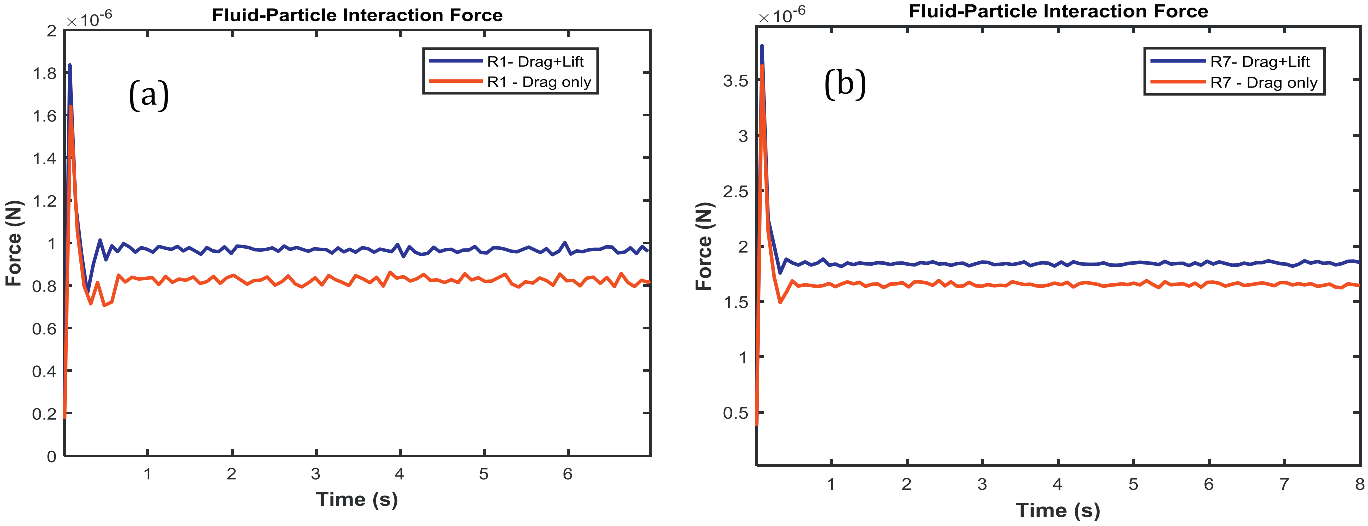

Fig. A4. Comparison of the average F–P forces with and without lift (a) R1(b) R7.

lift" case. Hence, the addition of lift force makes a difference when simulating F–P interaction a dilute system.

Fig. A4 shows a plot of the magnitude of the total F–P forces (average of the magnitude of the F–P force on each particle) for cases with and without lift force for (a) R1 and (b) R7. In both cases, the F–P forces are about 25% and 13% higher when lift forces are included for R1 and R7, respectively. This shows that inclusion of the lift force is important. Although the P–W and P–P interaction forces exceed the F–P interaction as shown in Figs. A1 and A2, the 20% difference in F–P interaction (R1) may be significant when simulating particle deposition, clustering, or re-entrainment. We therefore included the lift forces in all our simulation.

References

[1] J. Pisecky, Handbook of Milk Powder Manufacture, GEA Process Engineering A/S, Copenhagen, 2012.
[2] K.J. Hanley, P.E. Byrne, K. Cronin, C. Jorge, J.C. Oliveira, J. O'Mahony, A.M. Fenelon, Effect of pneumatic conveying parameters on physical quality characteristics of infant formula, J. Food Eng. 106 (2011) 236–244.
[3] I. Boiarkina, C. Sang, N. Depree, A. Prince-Pike, W. Yu, I.D. Wilson, R.B. Young, The significance of powder breakdown during conveying within industrial milk powder plants, J. Adv Powder Technol. 27 (2016) 2363–2369.
[4] K.J. Hanley, K. Cronin, C. O'Sullivan, M. Fenelon, J. O'Mahony, P.E. Byrne, Effect of composition on the mechanical response of agglomerates of infant formulae, J. Food Eng. 107 (1) (2011) 71–79.
[5] K.J. Hanley, K. Cronin, P.E. Byrne, Dispersion in particle velocity resulting from random motion through a spatially-varying fluid velocity field in a pipe, Powder Technol. 245 (2013) 255–264.
[6] K.L. Ostrowski, S.P. Luke, M.A. Bennett, R.A. Williams, Application of capacitance electrical tomography for on-line and off-line analysis of flow pattern in horizontal pipeline of pneumatic conveyer, Chem. Eng. J. 77 (1–2) (2000) 43–502000.
[7] C. Yang, Z. Cui, Q. Xue, H. Wang, D. Zhang, Y. Geng, Application of a high speed ECT system to online monitoring of pneumatic conveying process, Measurement 48 (2014) 29–42.
[8] F. Yan, A. Rinoshika, Application of high-speed PIV and image processing to measuring particle velocity and concentration in a horizontal pneumatic conveying with dune model, J. Powder Technol. 208 (2011) 158–165.
[9] M. Ebrahimi, M. Crapper, J.Y. Ooi, Experimental and simulation studies of dilute horizontal pneumatic conveying, J. Particulate Sci. and Technol. 32 (2) (2014) 206–213.
[10] S. Laín, M. Sommerfeld, A study of the pneumatic conveying of non-spherical particles in a turbulent horizontal channel flow, Braz. J. Chem. Eng. 24 (2007) 535–546.
[11] G.E. Klinzing, A simple light-sensitive meter for measurement of solid/gas loadings and flow steadiness, Ind. Eng. Chem. Process Des. Dev. 19 (1980) 31–33.
[12] A. Yilmaz, E.K. Levy, Formation and dispersion of ropes in pneumatic conveying, J. Powder Technol. 114 (2001) 168–185.
[13] A. Yilmaz, E.K. Levy, Roping phenomena in pulverized coal conveying lines, J. Powder Technol. 95 (1998) 43–48.
[14] Y.,E. Lim, C. Wang, Pneumatic transport of granular materials in an inclined conveying pipe: comparison of computational fluid dynamics-discrete element method (CFD-DEM), electrical capacitance tomography (ECT), and particle image velocimetry (PIV) results, Ind. Eng. Chem. Res. 46 (19) (2007) 6066–6083.
[15] K.W. Chu, B. Wang, A.B. Yu, A. Vince, G.D. Barnett, P.J. Barnett, CFD–DEM study of the effect of particle density distribution on the multiphase flow and performance of dense medium cyclone, J. Minerals Eng. 22 (2009) 893–909.
[16] S. Yuu, T. Umekage, Y. Johno, Numerical simulation of air and particle motions in bubbling fluidized bed of small particles, J. Powder Technol. 110 (2000) 158–168.
[17] Y.Q. Feng, B.H. Xu, S.J. Zhang, A.B. Yu, P. Zulli, Discrete particle simulation of gas fluidization of particle mixtures, AIChE J. 50 (2004) 1713–1728.
[18] T. Tsuji, K. Yabumoto, T. Tanaka, Spontaneous structures in three-dimensional bubbling gas fluidized bed by parallel DEM–CFD coupling simulation, J. Powder Technol. 184 (2008) 132–140.

[19] H. Ma, Y. Zhao, CFD-DEM investigation of the fluidization of binary mixtures containing rod-like particles and spherical particles in a fluidized bed, Powder Technol. 336 (2018) 533–545.
[20] B.H. Xu, Modelling of the gas fluidization of a mixture of cohesive and cohesionless particles by a combined continuum and discrete model, KONA 21 (2003) 100–108.
[21] D. Liu, B.G.M. van Wachem, R.F. Mudde, X. Chen, J.R. van Ommen, An adhesive CFD-DEM model for simulating nanoparticle agglomerate fluidization, AIChE J. 62 (7) (2016) 2259–2270.
[22] M. Afkhami, A. Hassanpour, M. Fairweather, D.O. Njobuenwu, Fully coupled LES-DEM of particle interaction and agglomeration in a turbulent channel flow, Comput. Chem. Eng. 78 (2015) 24–38.
[23] N. Almohammed, M. Breuer, Modelling and simulation of particle–wall adhesion of aerosol particles in particle-laden turbulent flows, Int. J. Multiph. Flow 85 (2016) 142–156.
[24] Z.B. Tong, Yu Yang, Y. R, B. A, CFD-DEM study of the aerosolisation mechanism of carrier-based formulations with high drug loadings, J. Powder Technol. 314 (2017) 620–626.
[25] H.E.A. Van den Akker, Mesoscale flow structures and fluid-particle interactions, in: Guy B. Marin, Jinghai Li (Eds.),Mesoscale Modelling in Chemical Engineering Part I, vol. 46, Academic Press, *UK* 2015, pp. 281–354 , Advances in Chemical Engineering.
[26] Ansys, Fluent Theory Guide, Ansys Inc., Canonsburg, PA, USA, 2017.
[27] H.M. Norouzi, R. Zarghami, R. Sotudeh-Gharebagh, N. Moustoufi, Coupled CFD-DEM Modelling: Formulation, Implementation and Application to Multiphase Flows, first ed. Wiley, 2016.
[28] G. Taguchi, System of Experimental Design: Engineering Methods to Optimize Quality and Minimize Costs, vols. 1–2, , UNIPUB/Kraus International Publications, New York, 1987.
[29] P.A. Cundall, O.D.L. Strack, A discrete numerical model for granular assemblies, Geotechnique 29 (1979) 47–65.
[30] Y. Tsuji, T. Tanaka, T. Ishida, Lagrangian numerical simulation of plug flow of cohesionless particles in a horizontal pipe, J. Powder Technol. 7 (1992) 239–250.
[31] Y. Tsuji, T. Kawaguchi, T. Tanaka, Discrete particle simulation of 2-dimensional fluidized-bed, J. Powder Technol. 77 (1993) 79–87.
[32] H.P. Zhu, Z.Y. Zhou, R.Y. Yang, A.B. Yu, Discrete particle simulation of particulate systems: theoretical developments, Chem. Eng. Sci. 62 (2007) 3378–3396.
[33] M. Ebrahimi, M. Crapper, CFD-DEM simulation of turbulence modulation in horizontal pneumatic, Particuology 31 (2017) 15–24.
[34] T.B. Anderson, R. Jackson, Fluid mechanical description of fluidized beds. Equations of motion, Ind. Eng. Chem. Fundam. 6 (4) (1967) 527–539.
[35] K. Rietema, H.E.A. Van den Akker, On the momentum equations in dispersed two phase systems, Int. J. Multiph. Flow 9 (1983) 21–36.
[36] V. Armenio, V. Fiorotto, The importance of the forces acting on particles in turbulent flows, J. Phys Fluids 13 (8) (2001) 2437–2440.
[37] A. Haider, O. Levenspiel, Drag coefficient and terminal velocity of spherical and non-spherical particles, J. Powder Technol. 58 (1989) 63–70.
[38] W. Zhong, A. Yu, X. Liu, Z. Tong, H. Zhang, DEM/CFD-DEM modelling of non-spherical particulate systems: theoretical developments and applications, J Powder Tech 302 (2016) 108–152.
[39] D.E.M. Solutions, Parallel EDEM-CFD Coupling for Ansys Fluent® – User Guide, DEM Solutions Ltd., Edinburgh, United Kingdom, 2015.
[40] J.B. McLaughlin, Aerosol particle deposition in numerically simulated channel flow, J. Phys. Fluids A: Fluid Dyn. (1) (1989) 1211–12241989-1993.
[41] P.G. Saffman, The lift on a small sphere in a slow shear flow, J. Fluid Mech. 22 (1965) 385–400.
[42] D.E.M. Solutions, EDEM 2017 User Guide–Creator, DEM Solutions Ltd., Edinburgh, United Kingdom, 2017.
[43] K.L. Johnson, K. Kendall, A.D. Roberts, Surface energy and the contact of elastic solids, Proceedings of the Royal Society of London. Series A 324 (1971) 301–313.
[44] L. Lapcik, B. Lapcikova, E. Otyepkova, M. Otyepka, J. Vlcek, F. Bunka, R.N. Salek, Surface energy analysis (SEA) and rheology of powder milk dairy products, J. Food Chem. 174 (2015) 25–30.
[45] P.C. Hiemenz, R. Rajagopalan, Principle of Colloid and Surface Chemistry, third ed. Marcel Dekker, Inc., New York, US, 1997.